This article has been accepted for inclusion in a future issue of this journal. Content is final as presented, with the exception of pagination.

Telegrapher Equation-Based FDTD Modeling of Multiport Nonreciprocal Resonator-Based RF Circuits

Anand Kumar, *Graduate Student Member, IEEE*, Zixiao Zhang, *Graduate Student Member, IEEE*, Debdeep Sarkar, *Senior Member, IEEE*, Symeon Nikolaou, *Senior Member, IEEE*, Photos Vryonides, *Senior Member, IEEE*, and Dimitra Psychogiou, *Senior Member, IEEE*

***Abstract*—This article presents a novel finite-difference time-domain (FDTD) framework for the analysis and design of multiport nonreciprocal (NR) circuits based on spatiotemporally modulated (STM) resonators. Traditional frequency-domain methods, such as harmonic balance (HB) simulations, face significant challenges in modeling time-modulated elements due to harmonic truncation. In contrast, the proposed time-domain (TD) approach inherently supports arbitrary waveforms and adaptive components, enabling accurate and efficient analysis of space–time-modulated and tunable RF systems. Specifically, the proposed FDTD-based analysis framework introduces a generalized update scheme for interconnected transmission line (TL) junctions and lumped-element resonators using modified Telegrapher's equations and custom boundary conditions (BCs), allowing to support complex circuit topologies, including NR-bandpass filters (NR-BPFs), NR-filtering power dividers (NR-FPDs), and NR-filtering couplers, and extract their key performance metrics such as TD waveforms, S-parameters, and constellation diagrams. Real-time simulations demonstrate the method's ability to model direction-dependent behavior, frequency conversion, and broadband signal propagation with high accuracy. The method is exhaustively compared and validated with simulations and measurements through the manufacturing and testing of three experimental prototypes at the UHF band. These include: 1) a tunable 3rd-order in-line NR-BPF; 2) a tunable 4th-order single-band NR-BPF; and 3) a 3rd-order NR-FPD.**

***Index Terms*—Filters, finite-difference time domain (FDTD), nonreciprocity, RF components, space–time modulation.**

Received 9 January 2026; revised 2 March 2026 and 22 March 2026; accepted 9 April 2026. This work was supported in part by Research Ireland under Project 20/RP/8334; in part by the Science and Engineering Research Board (SERB), Department of Science and Technology, Government of India, under Grant SRG/2021/000831; in part by the Prime Minister's Research Fellowship (PMRF), Ministry of Education, Government of India, under Grant TF/PMRF-22-3965; in part by the Cohesion Policy Funds "THALEIA 2021-2027" with EU Co-Funding under Grant BRIDGE2HORIZON/0823D/0005 (SWIFTWAVE); and in part by the ENTERPRISES/0223/Sub-Call0.576 ROMANIA Project co-funded by the Recovery and Resilience Facility of the Next Generation EU Instrument. *(Corresponding author: Anand Kumar.)*

Anand Kumar is with the Tyndall National Institute, University College Cork, Cork, T12 K8AF Ireland, and also with the Department of Electrical Communication Engineering, Indian Institute of Science, Bengaluru, Karnataka 560012, India (e-mail: anandkumar13@iisc.ac.in).

Zixiao Zhang and Dimitra Psychogiou are with the School of Engineering, University College Cork, Cork, T12 K8AF Ireland, and also with the Tyndall National Institute, Cork, T12 R5CP Ireland.

Debdeep Sarkar is with the Department of Electrical Communication Engineering, Indian Institute of Science, Bengaluru, Karnataka 560012, India (e-mail: debdeep@iisc.ac.in).

Symeon Nikolaou and Photos Vryonides are with the Frederick Research Centre, Frederick University, 1036 Nicosia, Cyprus (e-mail: s.nikolaou@frederick.ac.cy; p.vryonides@frederick.ac.cy).

Digital Object Identifier 10.1109/TMTT.2026.3683629

I. Introduction

NONRECIPROCAL (NR) RF circuits, such as isolators or circulators, are fundamental building blocks of RF front ends, enabling isolation and directional RF signal routing [1], [2], [3]. These functionalities are critical in radars and wireless communication applications, such as in-band full duplex (IFBD) and joint communication and sensing (JCAS), where directionality is essential to isolate RF signals at the same frequency band [4].

Conventional NR devices are based on ferrite materials [5], [6], [7] or magnetooptic effects [8]. However, they are bulky and hard to integrate with integrated circuits (ICs), creating significant interest in magnet-less implementations. These include acoustoelectric delay lines [9], magnetostatic surface waves in yttrium iron garnet (YIG) films [10], [11], asymmetric piezoelectric transducers [12], [13], FET-loaded resonators [14], [15], and modulated capacitive elements [16]. Among these approaches, spatiotemporally modulated (STM) resonators have emerged as a compelling approach, enabling NR filters [17], [18], [19], [20], [21], [22], [23], [24], NR-filtering power dividers (NR-FPDs) [25], and multielement communication systems like mixer-duplexer antennas [26], [27].

Modeling such systems is fairly cumbersome; frequency-domain techniques, such as harmonic balance (HB) [28], spectral admittance matrix (SAM) [17], and coupling matrix (CM) methods [18], require harmonic truncation, i.e., the limitation of the number of frequency harmonics considered, due to constraints on matrix size, processing time, and memory usage. This truncation reduces accuracy in strongly modulated scenarios, where many harmonics contribute significantly, and the resulting large matrix computations become increasingly time- and memory-intensive. Data-driven approaches such as deep neural networks (DNNs) were employed in [29] to model NR-bandpass filters (NR-BPFs), but they also depend on extensive HB simulations for training for individual circuits, limiting generality and scalability to higher order or multiport circuits.

Time-domain (TD) methods, particularly the finite-difference TD (FDTD) technique, provide a flexible alternative for analyzing NR-circuits, as they inherently capture transient behavior, arbitrary waveforms, and real-time system dynamics. FDTD has been previously applied to bulk time-modulated dielectrics [30], [31], [32], [33], [34], [35], [36], time-varying transmission lines (TVTLs) with in-line modulated capacitors [37], [38], [39], [40], and two-port NR filters with in-line *LC* resonators [41]. However, these implementations remain limited to simple in-line topologies and do not accommodate general multiport interconnections or transmission line (TL) junctions. More advanced FDTD variants [42], [43], [44], [45] introduce complex numerical constructs such as auxiliary potentials or unconditionally stable schemes, which can improve numerical stability or efficiency but add implementation overhead and obscure direct circuit-level interpretation (e.g., mapping computed voltages back to lumped elements or TL quantities). Moreover, these methods do not support time modulation of circuit elements. In contrast, the proposed formulation retains a direct correspondence between the FDTD state variables (voltages and currents) and the physical circuit elements (lumped inductors, capacitors, and TL sections), thereby enabling intuitive circuit-level interpretation and design insight while explicitly supporting time modulation of circuit elements. Existing frequency-domain approaches, such as HB and SAM, remain constrained by harmonic truncation and are inherently limited to periodic space–time modulation and steady-state analysis. To the best of the authors' knowledge, FDTD-based approaches capable of handling multiport STM circuits with stubs and junctions have not been demonstrated prior to this work.

To overcome the aforementioned limitations, this article presents a generalized FDTD-based framework for the analysis and design of multiport NR microwave circuits composed of STM resonators and interconnected TL junctions. The proposed method enables dynamic simulation of STM structures—including RF filters, directional couplers, power dividers, and resonant networks—without requiring harmonic truncation or steady-state assumptions. A conceptual illustration of the proposed FDTD-based computational electromagnetic (CEM) solver for analyzing multiport NR-circuits composed of time-modulated resonators and unmodulated resonators while supporting diverse excitation schemes is illustrated in Fig. 1. It can be utilized to analyze the performance of RF circuits with arbitrary complexity and extract both their time- and frequency-domain metrics, including S-parameters and modulated signal responses. Nonreciprocity is introduced by modulating the resonators with progressively phase-shifted low-frequency AC signals. The solver supports various excitations, including sinusoids, pulses, and arbitrary waveforms, and provides outputs such as TD waveforms, frequency spectra, S-parameters, and constellation diagrams for modulated signals like quadrature phase shift keying (QPSK). Specifically, the proposed FDTD modeling approach uniquely introduces the following.

1) A generalized TD solver for NR-circuits using FDTD and time-modulated lumped-element resonators.

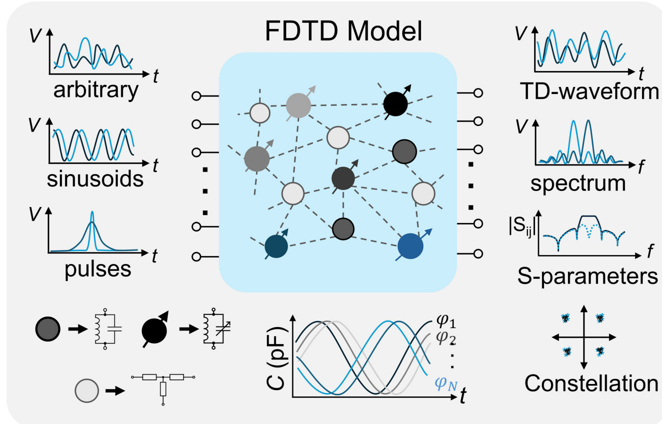

Fig. 1. Conceptual representation of the proposed FDTD-based CEM solver for the analysis of multiport, NR-circuits having STM resonators, static resonators, and nonresonating nodes.

2) A novel, TL-based junction modeling approach, based on modified Telegrapher's equations and custom boundary conditions (BCs).
3) Modeling of embedded lumped elements (e.g., inductors and capacitors), different types of resonators, and arbitrary waveforms, including modulated RF signals.
4) Extraction of TD and frequency-domain metrics (e.g., S-parameters, spectra, and constellation diagrams) from a single simulation run.

Unlike conventional HB-based circuit simulation methods, the proposed FDTD-based approach does not experience convergence issues with the increase of modulation strength as it enables full-wave transient analysis, captures all harmonics, and allows for a broadband simulation of STM circuits with high fidelity. It also supports excitation and modulation using arbitrary waveforms. This capability facilitates real-time evaluation of NR behavior such as direction-dependent filtering, frequency translation, modulation integrity, and testing with modulated signals such as QPSK and constellation diagrams—without requiring physical hardware.

Existing FDTD implementations for STM systems have primarily focused on bulk time-varying media, TVTLs, or two-port in-line resonator structures [30], [31], [32], [33], [34], [35], [36], [37], [38], [39], [40], [41]. These approaches, while effective for simple cascaded topologies, do not accommodate general multiport interconnections, multiconnected TL loops, or arbitrary junction configurations. The present Telegrapher's equation-based formulation extends prior work by explicitly incorporating junction BCs within the FDTD framework, thereby enabling scalable modeling of multiport NR-circuits with complex interconnections of time-modulated resonators. This unified treatment of STM resonators with TLs, stubs, and multiconnected junctions allows the analysis of circuit architectures that are not accessible using previously reported FDTD treatments of STM systems.

This article is organized as follows. Section II details the derivation of the FDTD equations and elaborates on the TL junction modeling. Section III describes the S-parameter extraction method. Section IV presents a validation of the

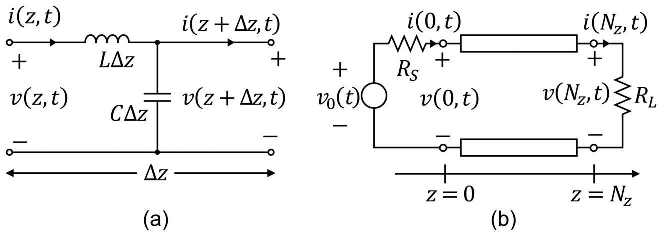

Fig. 2. (a) Incremental section of a lossless TL (TL-unit cell). (b) Simplified representation of a TL circuit in FDTD space with source and load.

TABLE I
KEY SYMBOLS AND INDICES USED IN THE FDTD FORMULATION

Symbol	Description
k	Spatial index along the TL
n	Temporal index (integer time steps for voltage)
$n+0.5$	Half-integer time steps for current; $t_{n+0.5}=(n-1/2)\,\Delta t$, $n=1,2,3,\ldots$
$k+0.5$	Half-integer spatial steps for current; $z_{k+0.5}=(k-1/2)\,\Delta z$, $k=1,2,\ldots$
v_k^n	Voltage at spatial node k, time step n
$i_{k+0.5}^{n+0.5}$	Current at spatial node $k+0.5$, time step $n+0.5$
L, C	Per-unit-length inductance and capacitance
Δz	Spatial discretization step
Δt	Temporal discretization step
R_S, R_L	Source and load resistances
$C_p(t)$	Time-modulated capacitor in LC resonator
$i_{LP,k}^n$	Current through parallel inductor L_p at node k, time n
L_m, C_m	PUL inductance/capacitance of main TL
L_s, C_s	PUL inductance/capacitance of stub TL
$i_{s,k}^n$	Stub current at junction node k, time n

FDTD method for various RF circuits with increased complexity, including RF filters, couplers, and dividers. Section V analyzes waveform-dependent responses, and Section VI reports on the experimental validation of the concept.

II. FDTD Update Equations for STM Circuits

This section derives the FDTD update equations for NR-circuits with time-modulated lumped elements and complex TL junctions. The formulation extends the classical telegrapher's equations to capture dynamic resonator behavior and multiconnected circuit topologies.

The formulation begins with the classical Telegrapher's equations for a lossless TL-unit cell, as shown in Fig. 2(a)

$$v(z+\Delta z,t) - v(z,t) + L\Delta z\frac{\partial i(z,t)}{\partial t} = 0 \tag{1a}$$

$$i(z,t) - i(z+\Delta z,t) - C\Delta z\frac{\partial v(z+\Delta z,t)}{\partial t} = 0 \tag{1b}$$

where L and C denote the inductance and capacitance per unit length (PUL), respectively. A summary of key symbols and indices used in the FDTD formulation is listed in Table I.

Discretization of (1) yields the standard FDTD updates

$$i_{k+0.5}^{n+0.5} = i_{k+0.5}^{n-0.5} - \left(\tfrac{\Delta t}{L\Delta z}\right)\left(v_{k+1}^n - v_k^n\right) \tag{2a}$$

$$v_k^{n+1} = v_k^n - \left(\tfrac{\Delta t}{C\Delta z}\right)\left(i_{k+0.5}^{n+0.5} - i_{k-0.5}^{n+0.5}\right) \tag{2b}$$

with $z = k\Delta z$ and $t = n\Delta t$.

From Fig. 2(b), at $k = 1$ and $k = N_z$, the update of v must be modified to incorporate the following BCs:

$$v_1^{n+1} = v_1^n - \tfrac{\Delta t}{C\Delta z}\left(i_{1.5}^{n+0.5} - i_{0.5}^{n+0.5}\right) \tag{3a}$$

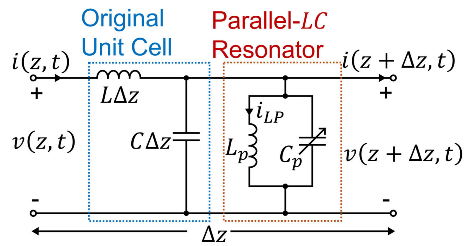

Fig. 3. Modified TL-unit cell for a parallel-LC resonator block with time variable resonant frequency caused by a time-modulated capacitor $C_p(t)$.

$$v_{N_z}^{n+1} = v_{N_z}^n - \tfrac{\Delta t}{C\Delta z}\left(i_{N_z+0.5}^{n+0.5} - i_{N_z-0.5}^{n+0.5}\right). \tag{3b}$$

For the source termination ($z = 0$)

$$v(0,t_n) + R_S\, i(0,t_n) = v_0(t_n) \tag{4}$$

with $v(0,t_n) = v_1^n$ and $i(0,t_n) \approx 1/2(i_{0.5}^{n+0.5} + i_{1.5}^{n+0.5})$, giving

$$i_{0.5}^{n+0.5} = -i_{1.5}^{n+0.5} - \tfrac{2}{R_S}v_1^n + \tfrac{2}{R_S}v_0(t_n). \tag{5}$$

The averaging of $i_{0.5}^{n+0.5}$ and $i_{1.5}^{n+0.5}$ provides the second-order accurate temporal and spatial centering at the boundary, as required by the staggered-grid leapfrog scheme. For the load termination ($z = h$)

$$v(h,t_n) - R_L i(h,t_n) = 0 \tag{6}$$

with $v(h,t_n) = v_{N_z}^n$ and $i(h,t_n) \approx 1/2(i_{N_z-0.5}^{n+0.5} + i_{N_z+0.5}^{n+0.5})$, giving

$$i_{N_z+0.5}^{n+0.5} = -i_{N_z-0.5}^{n+0.5} + \tfrac{2}{R_L}v_{N_z}^n. \tag{7}$$

Substituting these into the voltage update at $k = 1$ and $k = N_z$ yields

$$v_1^{n+1} = \left(1 - \tfrac{2\Delta t}{R_S C\Delta z}\right)v_1^n - \tfrac{2\Delta t}{C\Delta z}i_{1.5}^{n+0.5} + \tfrac{2\Delta t}{R_S C\Delta z}v_0(t_n) \tag{8a}$$

$$v_{N_z}^{n+1} = \left(1 - \tfrac{2\Delta t}{R_L C\Delta z}\right)v_{N_z}^n + \tfrac{2\Delta t}{C\Delta z}i_{N_z-0.5}^{n+0.5}. \tag{8b}$$

The initial conditions are $v(z,0) = i(z,0) = 0$, ensuring that v and i vanish for all grid points at $n \le 1$.

A. Time-Modulated LC Resonator

To facilitate the modeling of STM resonators, the TL-unit cell in Fig. 2(a) has been modified to include an inductor L_p and a time-modulated capacitor $C_p(t)$ as shown in Fig. 3. As such, its corresponding Telegrapher's equations can be modified to

$$v(z+\Delta z,t) - v(z,t) + L\Delta z\frac{\partial i(z,t)}{\partial t} = 0 \tag{9a}$$

$$i(z,t) - i(z+\Delta z,t) - \frac{\partial C_p(t)\, v(z+\Delta z,t)}{\partial t} - C\Delta z\frac{\partial v(z+\Delta z,t)}{\partial t} - i_{LP}(z+\Delta z,t) = 0 \tag{9b}$$

where i_{LP} is the current through L_p and is calculated by

$$i_{LP}(z+\Delta z,t) = \frac{1}{L_p}\int_{t_0}^{t} v(z+\Delta z,t)\,dt + i_{LP}(z+\Delta z,t_0). \tag{9c}$$

Hence, the FDTD update equations are as follows:

$$i_{k+0.5}^{n+0.5} = i_{k+0.5}^{n-0.5} - \left(\tfrac{\Delta t}{L\Delta z}\right)\left(v_{k+1}^n - v_k^n\right) \tag{10a}$$

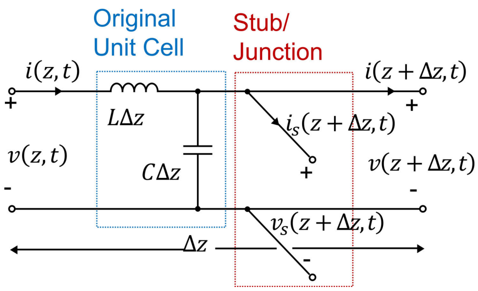

Fig. 4. Modified TL-unit cell to model a TL-junction or a stub on TL.

$$v_k^{n+1} = v_k^n - \left(\frac{\Delta t}{C\Delta z + C_p}\right)\left(i_{k+0.5}^{n+0.5} - i_{k-0.5}^{n+0.5} + i_{LP,k}^n\right) \tag{10b}$$

$$i_{LP,k}^{n+1} = i_{LP,k}^n + \left(\frac{\Delta t}{L_p}\right) v_k^n. \tag{10c}$$

Based on the above formulations, unit cells incorporating time-modulated inductors, or both time-modulated inductors and capacitors, can be modeled. However, while time-modulated capacitors can be practically realized using varactors driven by AC signals, a viable implementation for time-modulated inductors is not yet available. Therefore, this work focuses on demonstrating FDTD modeling techniques using time-modulated capacitors due to their practical viability.

B. TL Junctions

To facilitate junction modeling, the TL-unit cell is modified to include a stub/junction as shown in Fig. 4. Assuming that i_s is the current flowing through the stub and v_s is the voltage at the junction, the modified Telegrapher's equations are

$$v(z+\Delta z, t) - v(z,t) + L_m \Delta z \frac{\partial i(z,t)}{\partial t} = 0 \tag{11a}$$

$$i(z,t) - i(z+\Delta z, t) - C_m \Delta z \frac{\partial v(z+\Delta z, t)}{\partial t} - i_s(z+\Delta z, t) = 0. \tag{11b}$$

As such, the voltage and current in the stub can be updated using the Telegrapher's equations as

$$v_s(z+\Delta z, t) - v_s(z,t) + L_s \Delta z \frac{\partial i_s(z,t)}{\partial t} = 0 \tag{12a}$$

$$i_s(z,t) - i_s(z+\Delta z, t) - C_s \Delta z \frac{\partial v_s(z+\Delta z, t)}{\partial t} = 0 \tag{12b}$$

where v_s at the junction boundary is given by

$$v_s(z+\Delta z, t) = v(z+\Delta z, t) \tag{12c}$$

and the stub-end boundary can be set to an open-circuit, short-circuit, or impedance termination. Here, L_m and C_m are the PUL inductance and capacitance of the main TL, while L_s and C_s are the PUL inductance and capacitance of the stub TL. Thus, the FDTD update equations in the main TL and the stub-line are

$$i_{k+0.5}^{n+0.5} = i_{k+0.5}^{n-0.5} - \frac{\Delta t}{L_m \Delta z}\left(v_{k+1}^n - v_k^n\right) \tag{13a}$$

$$v_k^{n+1} = v_k^n - \frac{\Delta t}{C_m \Delta z}\left(i_{k+0.5}^{n+0.5} - i_{k-0.5}^{n+0.5} + i_{s,k}^n\right) \tag{13b}$$

$$i_{s,k+0.5}^{n+0.5} = i_{s,k+0.5}^{n-0.5} - \frac{\Delta t}{L_s \Delta z}\left(v_{k+1}^n - v_k^n\right) \tag{13c}$$

$$v_{s,k}^{n+1} = v_{s,k}^n - \frac{\Delta t}{C_s \Delta z}\left(i_{s,k+0.5}^{n+0.5} - i_{s,k-0.5}^{n+0.5} + i_{s,k}^n\right). \tag{13d}$$

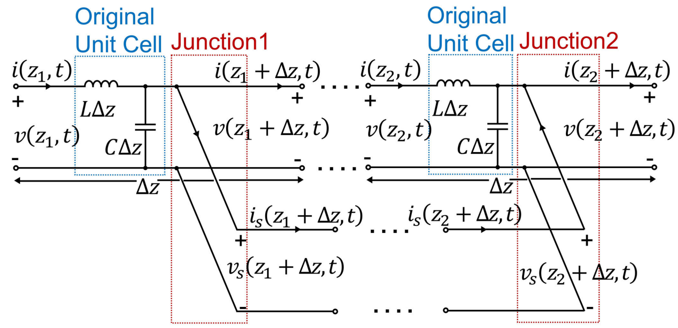

Fig. 5. Modified TL-unit cells to model a TL-based multiconnected junction. The parameters L and C denote PUL inductance and capacitance; for the main TL these are L_m, C_m and for the stub they are L_s, C_s.

The general update equations in (13) describe the coupled TD evolution of voltages and currents in the main TL and the attached stub-line. To complete the formulation, appropriate BCs must be specified at the termination of the stub, depending on the electrical load connected at its end. The following sub-subsections present the FDTD update equations for commonly encountered stub terminations, namely, resistive, open-circuit, and short-circuit loads as special cases derived directly from (13) by enforcing the corresponding terminal constraints.

1) Impedance Termination (R_L): For a termination with a resistive load R_L, the BC at $z = N_z$, from (8b), is

$$v_s(N_z, t) - R_L i_s(N_z, t) = 0 \tag{14}$$

Therefore:

$$v_{s,N_z}^{n+1} = \left(1 - \frac{2\Delta t}{R_L C_s \Delta z}\right) v_{s,N_z}^n + \left(\frac{2\Delta t}{C_s \Delta z}\right) i_{s,N_z-0.5}^{n+0.5}. \tag{15}$$

2) Open-Circuit Stub ($R_L \to \infty$): For an open-circuit load, $i_s = 0$ at $z = N_z$, i.e., $i_{s,N_z+0.5}^{n+0.5} = 0$ or $1/R_L \to 0$, from (15)

$$v_{s,N_z}^{n+1} = v_{s,N_z}^n + \left(\frac{2\Delta t}{C_s \Delta z}\right) i_{s,N_z-0.5}^{n+0.5}. \tag{16}$$

3) Short-Circuit Stub ($R_L \to 0$): For a short-circuit load

$$v_{s,N_z}^{n+1} = 0. \tag{17}$$

Beyond single-ended stub terminations, practical NR-circuits often include multiconnected TL sections forming loops or transversal interconnections. These configurations require additional junction BCs, as discussed next.

4) Multiconnected TL Junctions: To model circuits with multiconnected TL sections forming loops, the update equations in (11a)–(12b) need to be modified to have junction BCs at both ends of the stub-line. Consider the circuit in Fig. 5 with two modified TL-unit cells with junctions. The stub-TL is attached to the main-TL at two points, and hence the update equations at the two junctions must be modified.

Following the discussions above for (12a)–(12c), the modified Telegrapher's equations at junction 1 are:

$$v(z_1+\Delta z, t) - v(z_1,t) + L_m \Delta z \frac{\partial i(z_1,t)}{\partial t} = 0 \tag{18a}$$

$$i(z_1,t) - i(z_1+\Delta z, t) - C_m \Delta z \frac{\partial v(z_1+\Delta z, t)}{\partial t} - i_s(z_1+\Delta z, t) = 0 \tag{18b}$$

and for junction 2, (19b) is modified to account for the reversed direction of i_s. Hence, the modified Telegrapher's equations at junction 2 are

$$v(z_2+\Delta z,t)-v(z_2,t)+L_m\Delta z\frac{\partial i(z_2,t)}{\partial t}=0 \tag{19a}$$

$$i(z_2,t)-i(z_2+\Delta z,t) - C\Delta z\frac{\partial v(z_2+\Delta z,t)}{\partial t}+i_s(z_2+\Delta z,t)=0. \tag{19b}$$

Therefore, the FDTD update equations for (18a)–(19b) become

$$i_{k_1+0.5}^{n+0.5}=i_{k_1+0.5}^{n-0.5}-\frac{\Delta t}{L_m\Delta z}\left(v_{k_1+1}^{n}-v_{k_1}^{n}\right) \tag{20a}$$

$$v_{k_1}^{n+1}=v_{k_1}^{n}-\frac{\Delta t}{C_m\Delta z}\left(i_{k_1+0.5}^{n+0.5}-i_{k_1-0.5}^{n+0.5}+i_{s,k_1}^{n}\right) \tag{20b}$$

$$i_{k_2+0.5}^{n+0.5}=i_{k_2+0.5}^{n-0.5}-\frac{\Delta t}{L_m\Delta z}\left(v_{k_2+1}^{n}-v_{k_2}^{n}\right) \tag{21a}$$

$$v_{k_2}^{n+1}=v_{k_2}^{n}-\frac{\Delta t}{C_m\Delta z}\left(i_{k_2+0.5}^{n+0.5}-i_{k_2-0.5}^{n+0.5}-i_{s,k_2}^{n}\right). \tag{21b}$$

The voltages and currents in the stub-TL are updated using (13c) and (13d) with the following junction BCs:

$$v_s(z_1+\Delta z,t)=v(z_1+\Delta z,t) \tag{22a}$$

$$v_s(z_2+\Delta z,t)=v(z_2+\Delta z,t). \tag{22b}$$

The proposed FDTD scheme adheres to the Courant–Friedrichs–Lewy (CFL) stability criterion: $\Delta t \leq (\Delta z)/(v_{\max})$, where $v_{\max}$ is the maximum phase velocity. For time-modulated networks, $v_{\max}$ is calculated from the smallest effective inductance and capacitance values ($v_{\max}=1/(L_{\text{eff}}C_{\text{eff}})^{1/2}$) that occur during modulation. To ensure spectral accuracy up to a maximum frequency $f_{\max}$, the spatial step must satisfy $\Delta z \leq v_{\max}/(N_\lambda f_{\max})$, where N_λ is the number of points per wavelength (typically 10–20). The time step Δt is then chosen based on the CFL limit. Numerical tests performed under relatively strong modulation indices and high modulation frequencies indicate that, while extreme modulation parameters may affect the physical NR response, the numerical stability of the FDTD scheme remains unaffected provided that the CFL condition is satisfied.

Losses can be incorporated by starting from the lossy Telegrapher's equations with ohmic and dielectric losses, R and G, respectively, resulting in modified update equations that include damping terms without altering the CFL stability bound. Nonlinear effects may be introduced by modeling inductance or capacitance as voltage-dependent quantities, following established nonlinear FDTD approaches such as [46]. Although this increases computational overhead due to auxiliary update relations, it does not fundamentally modify the stability constraint. Since the formulation operates at the circuit level, parasitic effects can be explicitly included as lumped or distributed components within the FDTD network representation.

Considering both the time-modulated resonator formulations introduced earlier in this section and the junction modeling developed above, the resulting FDTD framework extends the classical Telegrapher's equations to support TL circuits with dynamic lumped elements and multiconnected topologies. This combined formulation forms the basis for analyzing multiport NR systems in the time and frequency domains, as demonstrated in the following.

Algorithm 1 S-Parameter Extraction of N-Port NR-Circuits Using FDTD

Initialization: Define circuit parameters, set $Z_0 = 50\ \Omega$ at all ports, and specify excitation frequencies $\{f_{\text{in}}\}$.
for each frequency f_{in} **do**
  for each input port $j = 1,\ldots,N$ **do**
    Excite port j with a truncated or Gaussian-modulated sinusoid at f_{in}.
    Run FDTD simulation and record $V_i(t), I_i(t)$ at all ports.
    Perform FFT to obtain $V_i(f_{\text{in}}), I_i(f_{\text{in}})$.
    Compute a_i, b_i using (23).
    Evaluate $S_{ij}(f_{\text{in}})$ using (24).
  end for
end for
Results: Assemble the full $N \times N$ S-parameter matrix across all f_{in}.

III. S-Parameters Analysis of NR Multiport RF Circuits

To calculate the S-parameters of such NR-RF circuit, the simulation domain needs to be terminated with a characteristic impedance $Z_0 = 50\,\Omega$ at all ports, and each port is excited individually with a sinusoidal source at a specified frequency f_{in}. Due to the use of time-modulated resonators in the NR-circuits, which induce frequency conversion and generate intermodulation products [1], traditional wideband excitation methods (e.g., Gaussian or sinc pulses) are inadequate. Therefore, a frequency-by-frequency approach is adopted in this case, where FDTD simulations are executed separately for each desired excitation frequency f_{in}. Specifically, the FDTD model is excited with a truncated sinusoid or Gaussian-modulated sinusoid at f_{in} for a duration of $n_{\text{cycles}} \times t_p$, where t_p is the propagation time required for the wave to travel from the source to the load and n_{cycles} is the number of times a pulse bounces between the source and the load. A higher n_{cycles} provides more TD data, improving the FFT accuracy and thus the accuracy of the extracted S-parameters. Typically, n_{cycles} is chosen to be approximately 100.

During each simulation, the complex phasors V_i and I_i at f_{in} are obtained by applying an FFT to the recorded TD port voltages $v_i(t)$ and currents $i_i(t)$, i.e., $V_i(f_{\text{in}}) = \mathcal{F}\{v_i(t)\}\,|_{f=f_{\text{in}}}$ and $I_i(f_{\text{in}}) = \mathcal{F}\{i_i(t)\}\,|_{f=f_{\text{in}}}$. The incident ($a_i$) and reflected ($b_i$) wave quantities are computed using the following relationships:

$$a_i=\frac{V_i+Z_0I_i}{2\sqrt{Z_0}},\quad b_i=\frac{V_i-Z_0I_i}{2\sqrt{Z_0}}. \tag{23}$$

The S-parameters at f_{in} are then obtained from the ratio

$$S_{ij}(f_{\text{in}})=\left.\frac{b_i(f_{\text{in}})}{a_j(f_{\text{in}})}\right|_{a_{j\neq i}=0} \tag{24}$$

where a_j is the excitation applied to port j, and all other incident waves a_i are set to zero, ensuring a single-port excitation condition. The corresponding S-parameter extraction procedure is summarized in Algorithm 1.

Having established the S-parameter extraction methodology, the capabilities of the proposed FDTD framework are

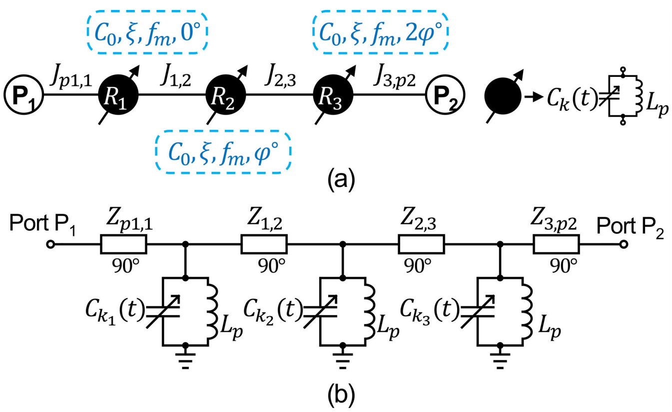

Fig. 6. (a) CRD and (b) circuit representation of a 3rd-order in-line NR-BPF comprising three STM in-line resonators. White circles: nonresonating nodes for the RF input/output, black circles: STM parallel *LC* resonators with phase-shifted low-frequency AC signals, black lines: impedance inverters.

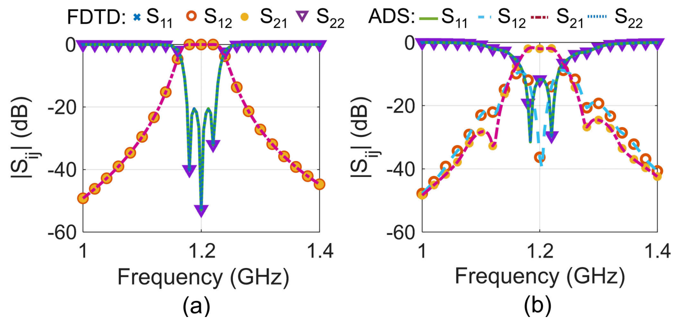

Fig. 7. S-parameters of the 3rd-order in-line NR-BPF in Fig. 6 using the proposed FDTD method and HB simulations. (a) Unmodulated (reciprocal) and (b) modulated (NR).

demonstrated next through several example NR-circuits, including NR-BPFs, NR-FPDs, and NR-filtering couplers—all incorporating time-modulated resonators.

IV. FDTD Simulations of NR Multiport Circuits

This section presents a series of circuit implementations to validate the proposed FDTD framework in MATLAB across a diverse set of NR-filtering structures with increasing circuit design complexity and number of ports. The examples are organized into three main categories: 1) NR-BPFs; 2) NR-FPDs; and 3) NR-filtering couplers. Each example includes a description of the circuit topology, governing equations, simulation setup, and the RF performance comparison between the proposed FDTD method and conventional HB simulations in ADS Keysight, both simulated with a 1-MHz frequency step.

The proposed FDTD framework serves as a complete simulation engine, analogous to a commercial solver such as Keysight ADS, capable of simulating, verifying, and optimizing NR-circuit designs within a single run while natively supporting time-modulated elements and arbitrary waveform excitations that frequency-domain tools cannot accommodate. The typical design flow begins with standard synthesis procedures [47] to determine the unmodulated circuit topology and element values. Time modulation is then applied to the *LC* resonator capacitances, and the modulation parameters are tuned to maximize NR performance following [17], [24].

A. NR-BPF Based on STM Resonators

In-line NR-BPFs are implemented using STM resonators that are connected in series through impedance inverters, while transversal NR-BPFs are based on transversal resonator doublets to enable sophisticated filtering responses. To demonstrate the applicability of the proposed FDTD-based method to modeling these types of filters, two representative examples of a three-resonator (3rd-order) in-line NR-BPF and a transversal four-resonator (4th-order) NR-BPF are discussed next:

1) Example 1—Third-Order In-Line NR-BPF: Fig. 6 illustrates the coupling routing diagram (CRD) and circuit schematic equivalent for a 3rd-order NR-BPF based on in-line STM. It consists of three STM resonators (R_1–R_3), which are represented by black circles with arrows. Each resonator can be modeled as a parallel *LC* tank consisting of a fixed value inductor L_p and a time-modulated capacitor, where C_k is the nominal capacitance, f_m is the modulation signal frequency, ξ_k is the modulation index, and ϕ_k is the modulation phase for the kth resonator. To establish NR transmission, a progressive modulation phase shift is applied along the signal path, enabling the desired spatiotemporal modulation effect [24]. In this example, all resonators share identical nominal capacitance, modulation index, and modulation frequency, while adjacent resonators are phase-shifted by ϕ, as labeled in blue in Fig. 6

$$C_k(t) = C_0 \left(1 + \xi \cos\left(2\pi f_m t + (k-1)\phi\right)\right), \quad k = 1, 2, 3. \tag{25}$$

In the FDTD model, resonators R_1–R_3 are modeled using the *LC*-resonator blocks in Fig. 3, governed by (10), while the impedance inverters J_{ij} are modeled using 90° TL sections, as shown in Fig. 2(a), with impedance Z_{ij} and the boundaries at Ports 1 and 2 are terminated by (8a) and (8b), respectively. The FDTD simulation was performed using the following circuit parameters: $Z_{P_1,1} = Z_{3,P_2} = 32.26\,\Omega$, $Z_{1,2} = Z_{2,3} = 37.04\,\Omega$, $C_0 = 97.72$ pF, $L_p = 0.18$ nH, $\xi = 0.094$, $f_m = 53$ MHz, and $\phi = 44°$. These parameters yield a center frequency f_{cen} of 1.2 GHz with a fractional bandwidth (FBW) of 0.07. The resulting S-parameters, obtained via the 1D-FDTD model, are shown in Fig. 7 under unmodulated (reciprocal) and modulated (NR) cases. The results exhibit strong agreement with HB simulations in Keysight ADS, thus verifying the validity and accuracy of the proposed FDTD-based methodology.

2) Example 2—Transversal Fourth-Order Single-Band NR-BPF: Fig. 8 illustrates the CRD of a transversal 4th-order NR-BPF and its equivalent circuit schematic whose basic operating principles are discussed in [24]. As it can be seen in the CRD in Fig. 8, R_2 and R_5, interface with multiple TL junctions and can be modeled using (10), (20), and (21), where (22a) is applied to R_2 and (22b) is applied to R_5. Resonators R_3 and R_4 follow the standard resonator formulation in (10), and all impedance inverters J_{ij} are modeled using 90° TL sections with characteristic impedance Z_{ij}, except J_{45}, which has a negative coupling value and uses a 270° TL section.

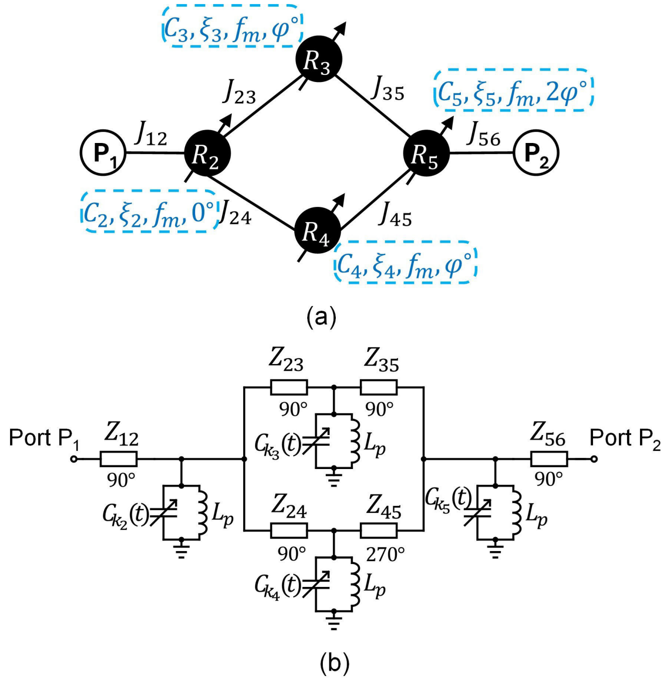

Fig. 8. (a) CRD and (b) circuit of a transversal 4th-order single-band NR-BPF comprising four STM resonators.

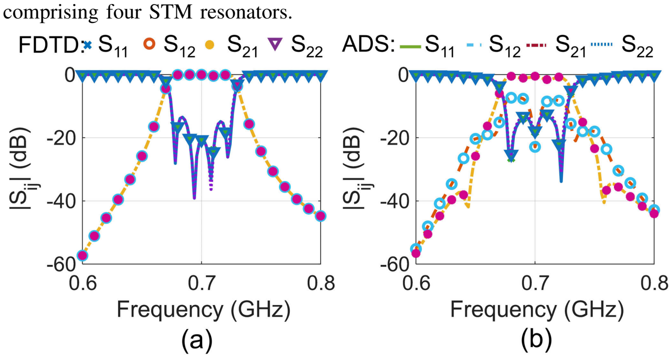

Fig. 9. S-parameters of the transversal 4th-order single-band NR-BPF in Fig. 8 using the proposed FDTD method and HB simulations. (a) Unmodulated (reciprocal) and (b) modulated (NR).

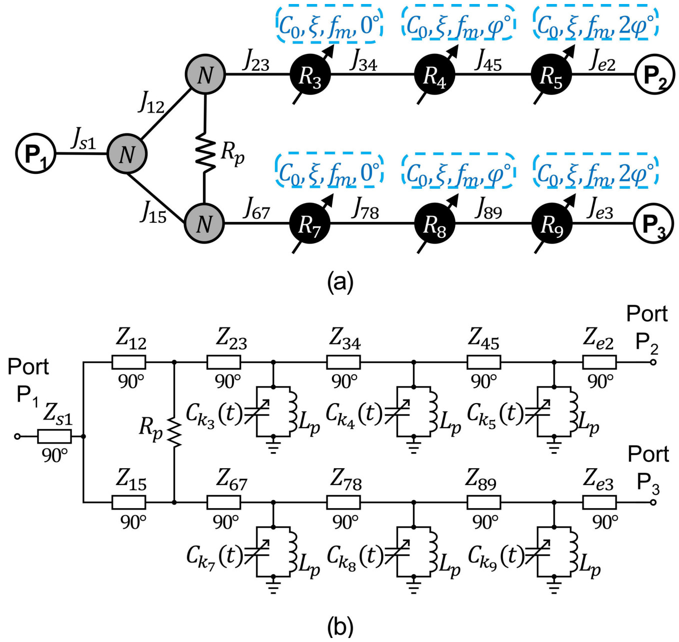

Fig. 10. (a) CRD and (b) circuit of a 3rd-order in-line NR-FPD. White circles: nonresonating nodes for the RF input/output, black circles: STM parallel-*LC* resonators with phase-shifted low-frequency AC signals, and gray circles: nonresonating nodes.

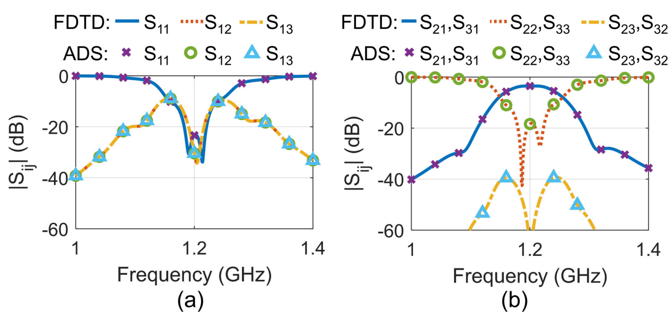

Fig. 11. S-parameters of the 3rd-order in-line NR-FPD (Fig. 10) using the proposed FDTD method and HB simulations. (a) $|S_{1j}|$ and (b) $|S_{2j}|, |S_{3j}|$, $j = 1, 2, 3$.

The transversal 4th-order NR-BPF was designed for f_{cen} of 700 MHz and an FBW of 9%. Specifically, the TL impedances were set as $Z_{12} = Z_{56} = 146.93\,\Omega$, $Z_{23} = Z_{35} = 718.14\,\Omega$, and $Z_{24} = Z_{45} = 736.54\,\Omega$. The capacitances were set to $C_2 = C_5 = 6.68$ pF, $C_3 = 7.025$ pF, and $C_4 = 6.35$ pF, while the inductance was fixed at $L_p = 7.74$ nH. Time modulation parameters included modulation indices $\xi_1 = \xi_4 = 0.075$ and $\xi_2 = \xi_3 = 0.058$, with a modulation frequency $f_m = 29$ MHz and phase offset $\phi = 70°$. Fig. 9 presents the S-parameter response obtained from the FDTD simulation under both unmodulated (reciprocal) and modulated (NR) scenarios. The results show excellent correlation with HB simulations performed in Keysight ADS, thereby confirming the fidelity and effectiveness of the proposed 1D-FDTD modeling approach.

B. NR-Filtering Power Divider

To validate the method's scalability in multiport NR-filtering networks, NR-FPDs using in-line and transversal topologies are analyzed in this section.

1) Example 1—Third-Order In-Line NR-FPD: To demonstrate the applicability of the proposed FDTD method to multiport NR-filtering, an NR-FPD based on a Wilkinson power divider with coupled resonators (Fig. 10) using a similar CRD as the one discussed in [33] was analyzed. The time-modulated resonators R_3–R_5 and R_7–R_9, similar to the previous circuits, were modeled using (10), (20), and (21), with nonresonating nodes N modeled by (13) to accommodate the TL junction. The inclusion of resistor R_p was handled by adjusting the current at the TL junctions connecting R_p. To evaluate the FDTD model, the NR-FPD was designed at 1.2 GHz with 7% FBW, using $Z_{s1} = 50\,\Omega$, $Z_{12} = Z_{16} = 74\,\Omega$, $Z_{23} = Z_{67} = Z_{e2} = Z_{e3} = 651.4\,\Omega$, $Z_{34} = Z_{45} = Z_{78} = Z_{89} = 168.12\,\Omega$, $R_p = 100\,\Omega$, $C_0 = 2.77$ pF, $L_p = 6.35$ nH, $\xi = 0.11$, $f_m = 65$ MHz, and $\phi = 60°$. Fig. 11 compares the FDTD and HB simulation results, showing excellent agreement and clearly illustrating the filter's NR response.

2) Example 2—Transversal Cell-Based NR-FPD: To further assess the scalability of the proposed FDTD approach, a more intricate NR-FPD was analyzed using a transversal

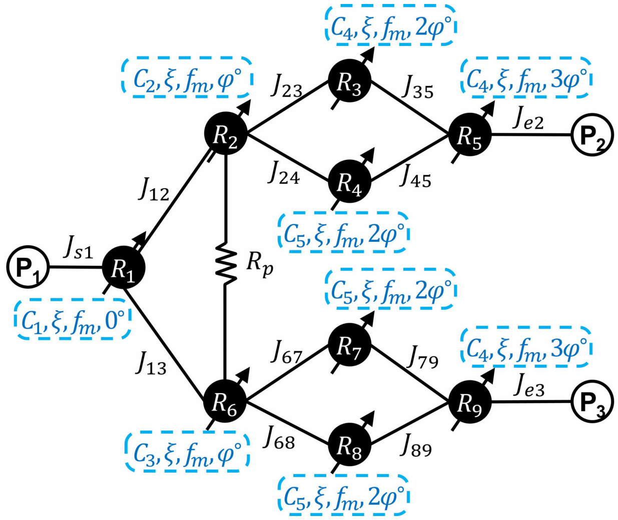

Fig. 12. CRD for an NR-FPD comprising transversal STM resonators.

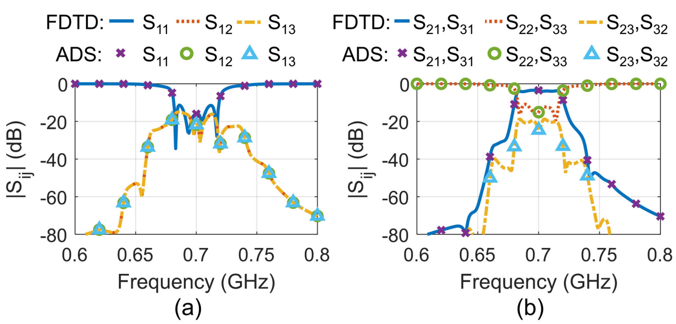

Fig. 13. S-parameters of the NR-FPD with transversal resonators in Fig. 12 using the proposed FDTD method and HB simulations. (a) $|S_{1j}|$ and (b)$|S_{2j}|$, $|S_{3j}|$, $j = 1, 2, 3$.

cell-based topology comprising nine STM resonators and multiple TL junctions (Fig. 12). Unlike simpler configurations, this circuit introduces additional design challenges such as several multiconnected TL junctions and STM resonators, and multiple phase offsets across the resonators. The FDTD implementation accounted for these complexities by implementing the modified update equations in (10), (13), (20), and (21) at resonators R_1, R_2, R_5, R_6, and R_9 to reflect the presence of TL junctions. Resistive elements R_p between R_2 and R_6 were incorporated through current adjustments at their respective junctions. The modulation phases were distributed to enable reconfigurable behavior: R_1 at 0°, R_2 and R_6 at ϕ, R_3, R_4, R_7, and R_8 at 2ϕ, and R_5 and R_9 at 3ϕ.

Targeting a center frequency of 700 MHz and 7% FBW, the circuit was designed using the following circuit parameters: $Z_{s1} = 97.33\,\Omega$, $Z_{12} = Z_{13} = 317\,\Omega$, $Z_{23} = Z_{67} = 396.15\,\Omega$, $Z_{24} = Z_{68} = 488.76\,\Omega$, $Z_{35} = Z_{79} = 296.9\,\Omega$, $Z_{45} = Z_{89} = 357.06\,\Omega$, and $Z_{e2} = Z_{e3} = 98.12\,\Omega$. The lumped elements were set to $C_1 = C_2 = C_5 = C_6 = C_9 = 23.18$ pF, $C_3 = C_7 = 22.58$ pF, $C_4 = C_8 = 24.06$ pF, $L_p = 2.23$ nH, and $R_p = 100\,\Omega$, with modulation parameters $\xi_k = 0.043$, $f_m = 20.5$ MHz, and $\phi = 50°$. All TL segments were 90°, except for J_{35} and J_{79}, which were implemented as 270° sections to enable negative coupling. The S-parameters plotted in Fig. 13 confirm the successful implementation, with simulation results aligning closely with HB data from Keysight ADS. The observed NR behavior further validates the model's capability to handle structurally complex and highly coupled NR networks.

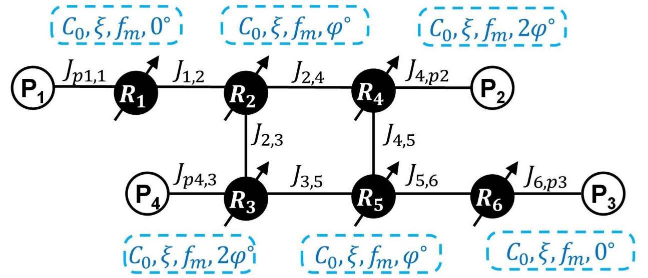

Fig. 14. CRD for a 3rd-order in-line NR-filtering 3-dB coupler using STM resonators.

C. Third-Order In-Line NR-Filtering 3-dB Coupler

To further illustrate the capabilities of the proposed method to simulate multiport circuits, a 3rd-order in-line NR-filtering 3-dB coupler was analyzed using the proposed FDTD approach. Its CRD is shown in Fig. 14 and its details have been extensively discussed in [48].

In this case, port P_1 serves as the input, ports P_2 and P_4 function as output ports, and port P_3 remains isolated. Conversely, when the input is applied at P_3, Ports P_2 and P_4 act as output ports with port P_1 serving as the isolation port. The design integrates six resonators (R_1–R_6) interconnected via impedance inverters J_{ij} and phase-managed paths to achieve simultaneous bandpass filtering and NR signal transmission. Resonators R_1–R_6 are arranged to form a coupled-resonator network. Each resonator operates at the center frequency f_{cen}, with couplings tuned to enforce a 3rd-order bandpass response. For the FDTD model, the resonators R_1 and R_6 were implemented using (10), R_2–R_5 were implemented using (20) and (21) in conjunction with (10), and the impedance inverters $J_{i,j}$ were implemented using 90° TL sections with impedance $Z_{i,j}$, except for $J_{4,5}$, which has a negative coupling coefficient and is implemented by 270° TL section. The NR-filtering coupler was designed for a center frequency of 700 MHz with an FBW of 5%. The circuit parameters are as follows: $Z_{P_{1},1} = Z_{4,P_2} = Z_{p4,3} = Z_{6,P_3} = 83.8\,\Omega$, $Z_{1,2} = Z_{5,6} = 161.25\,\Omega$, $Z_{2,4} = Z_{3,5} = Z_{2,3} = Z_{4,5} = 225.14\,\Omega$, $C_0 = 20.678$ pF, $L_p = 2.5$ nH, $\xi = 0.09$, $f_m = 33$ MHz and $\phi = 65°$. The resulting S-parameters, shown in Fig. 15, are compared against HB simulations from Keysight ADS, and as it can be seen, they exhibit a strong agreement.

V. Real-Time/TD Analysis

One of the key merits of the proposed FDTD method is that it can be used to simulate real-time testing of NR-circuits, allowing for a comprehensive evaluation of their performance in different types of TD signals. To demonstrate its potential, the aforementioned NR-circuit designs are analyzed in this section, highlighting the versatility of the FDTD model in simulating NR-RF circuits without the need for costly and

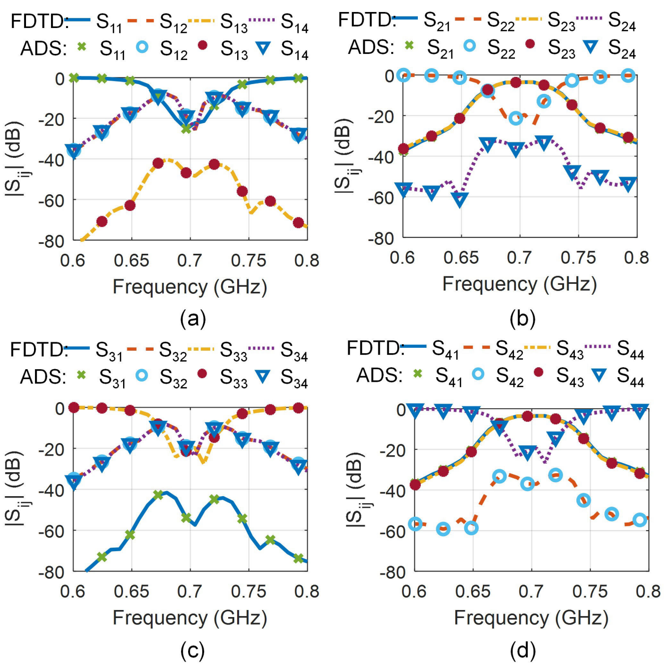

Fig. 15. S-parameters of the 3rd-order in-line NR 3-dB coupler in Fig. 14 using the proposed FDTD method and HB simulations. (a) $|S_{1j}|$, (b) $|S_{2j}|$, (c) $|S_{3j}|$, and (d) $|S_{4j}|$, $j = 1, 2, 3, 4$.

Algorithm 2 FDTD Analysis of N-Port NR-Circuit With Sinusoidal/Pulse Excitation

Initialization: Define circuit parameters, excitation type (sinusoid or pulse), and FDTD update coefficients.
for each input port $p = 1, 2, \ldots, N$ **do**
  Apply excitation (sinusoid or pulse) at port p.
  Run FDTD simulation and record TD response at all ports.
  for each output port $q = 1, 2, \ldots, N$ **do**
    Plot TD signal $v_q(t)$.
    Perform FFT on $v_q(t)$ to obtain $V_q(f)$.
    Plot frequency-domain spectrum $|V_q(f)|$.
  end for
end for
Results: Display TD responses and spectra for all port pairs (p, q).

time-intensive prototyping. For brevity, two circuits are analyzed, subjected to three different types of signals: sinusoidal, pulse, and QPSK signals.

A. Transversal Fourth-Order Single-Band NR-BPF

1) Sinusoidal Signal Analysis: The transversal 4th-order single-band NR-BPF in Fig. 8 is evaluated using continuous-wave signals at 700 MHz (in-band) and 650 MHz (out-of-band). The FDTD procedure for sinusoidal/pulse signal excitation and spectral extraction via FFT on the TD signals is summarized in Algorithm 2. In the forward direction ($P_1 \rightarrow P_2$), the 700-MHz signal is transmitted with minimal attenuation, while the reverse signal is significantly suppressed, as observed in Fig. 16(b) and (d), confirming strong

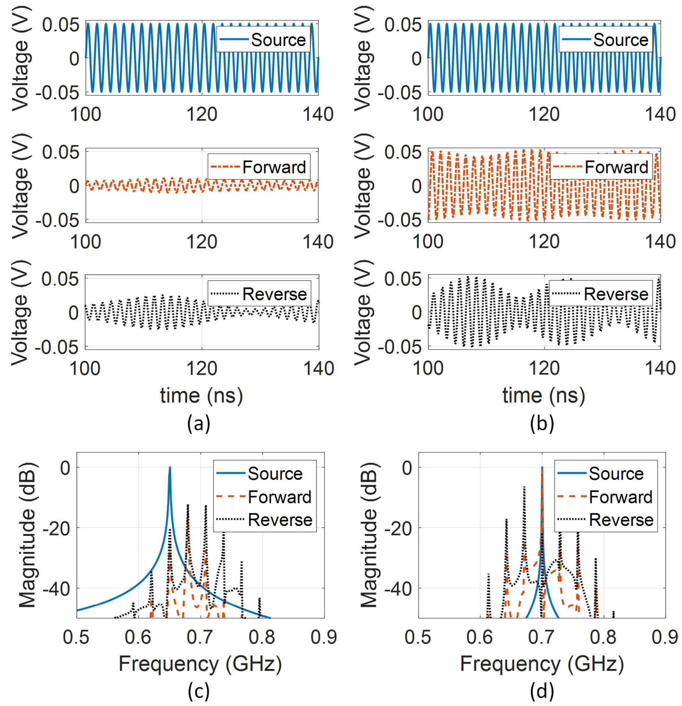

Fig. 16. Time- and frequency-domain responses of the transversal 4th-order single-band NR-BPF in Fig. 8 to sinusoidal inputs at 650 MHz (out-of-band, left column) and 700 MHz (in-band, right column). (a) and (b) TD waveforms and (c) and (d) corresponding spectra showing out-of-band rejection and in-band nonreciprocity.

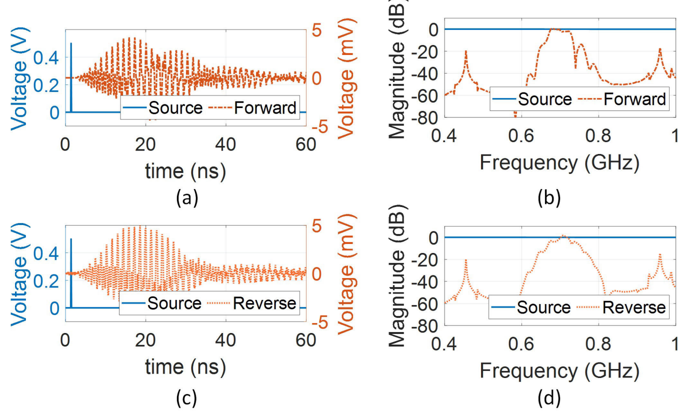

Fig. 17. Time- and frequency-domain responses of the transversal 4th-order single-band NR-BPF in Fig. 8 to a Gaussian pulse. (a) and (c) Real-time signals for forward and reverse propagation, and (b) and (d) their frequency spectra.

NR behavior. At 650 MHz, being outside the passband, the RF signals are attenuated in both directions, which explains the small observed magnitude [Fig. 16(a) and (c)], demonstrating effective frequency selectivity. Additionally, weak harmonic peaks are observed in the spectral plots, attributed to the spatiotemporal modulation of the resonators. These peaks are direction-dependent, validating the NR nature of the filter.

2) Pulse Signal Analysis: A TD Gaussian pulse is used to probe the broadband performance of the transversal 4th-order single-band NR-BPF. In the forward path (from P_1 to P_2), the output retains a distinguishable waveform [Fig. 17(a)] with several frequency components, and the corresponding spectrum is confined largely within the passband [Fig. 17(b)].

Algorithm 3 FDTD Analysis of N-Port NR-Circuit With QPSK Signal

Initialization: Define circuit, modulation, and source parameters; set up FDTD grid and update coefficients.
QPSK Signal Generation: Generate random bits, map to QPSK symbols, form waveform, add noise, and interpolate to FDTD time step; plot transmitted constellation.
for each input port $p = 1, 2, \ldots, N$ **do**
  Run FDTD simulation with excitation at port p.
  for each output port $q \neq p$ **do**
    Extract received signal at port q.
    Demodulate QPSK, recover bits, and compute BER.
    Plot received constellation and spectra.
  end for
end for
Results: Report BER for all port pairs (p, q), along with constellations, TD signals, and spectra.

In the reverse direction (from P_2 to P_1), the output waveform [Fig. 17(c)] is also similar, but with a broadened spectrum [Fig. 17(d)]. This asymmetry stems from the filter's frequency conversion capability via spatiotemporal modulation. Because a Gaussian pulse contains a wide range of frequency components, effectively spanning a broad spectrum, its interaction with the modulated resonators leads to spectral redistribution. The time-varying circuit parameters generate frequency-shifted harmonics, causing energy to leak both within and beyond the filter's intended passband. As a result, complete signal suppression in the reverse direction is not achieved, and some signal components are partially transmitted despite the filter's NR nature.

3) QPSK Signal Analysis: The performance of the NR-BPF was evaluated using QPSK-modulated signals to assess its behavior under realistic communication scenarios. The algorithm for QPSK implementation with the FDTD method is shown in Algorithm 3. An array of N_{bits} bits is mapped to QPSK symbols to form a waveform at f_{cen} and then used as excitation in the FDTD simulation. The received signal is then demodulated, and the bits are recovered to compute the bit error rate (BER) and plot constellation diagrams. As shown in Fig. 18, for $N = 200$ and $f_{cen} = 700$ MHz, the NR-BPF exhibits clear NR characteristics, evident from the pronounced difference in attenuation and spectral content between forward and reverse propagation. The input QPSK waveform and its spectrum are shown in Fig. 18(a) and (b), respectively. In the forward direction ($P_1 \rightarrow P_2$), the output waveform [Fig. 18(c)] and spectrum [Fig. 18(d)] demonstrate strong in-band transmission with minimal distortion. The constellation diagram at the output [Fig. 19(b)] remains well-defined with a BER of 0 and closely resembles the original [Fig. 19(a)], indicating that the filter maintains the amplitude, phase, and timing characteristics of the modulated signal, thus preserving signal integrity in the forward path. Conversely, in the reverse direction ($P_2 \rightarrow P_1$), the output signal experiences significant attenuation [Fig. 18(e)], accompanied by spectral degradation [Fig. 18(f)] and a severely distorted constellation [Fig. 19(c)] with BER equal to 0.625. These results confirm that the NR-BPF selectively allows clean signal transmission in one direction while suppressing and distorting signals in the reverse, making it a promising candidate for full-duplex communication systems requiring directional signal isolation and interference suppression.

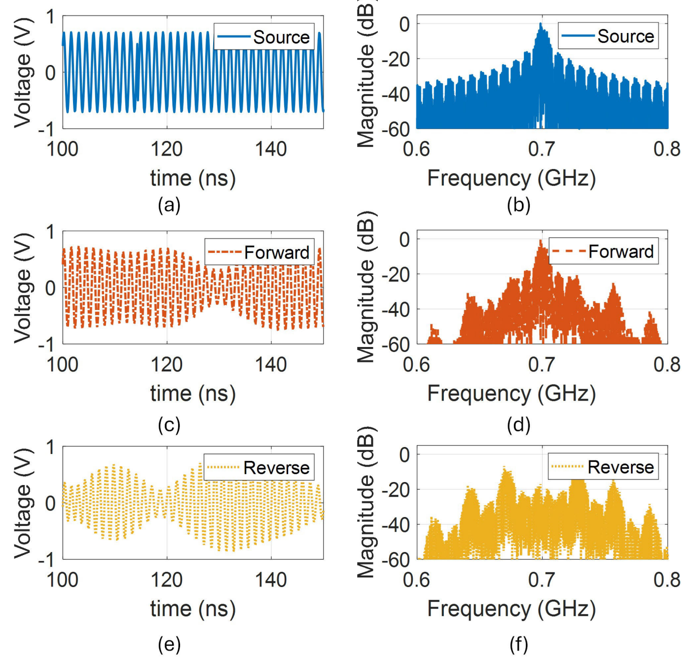

Fig. 18. Time- and frequency-domain responses of the transversal 4th-order single-band NR-BPF to a QPSK-modulated signal. (a) and (b) Source signal, (c) and (d) signal received in forward direction, and (e) and (f) signal received in reverse direction.

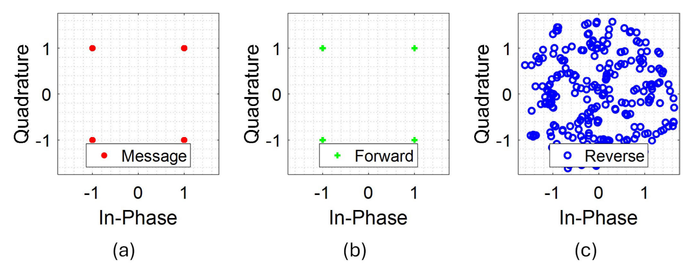

Fig. 19. QPSK constellation diagrams for the transversal 4th-order single-band NR-BPF. (a) Message signal, (b) forward, and (c) reverse propagation.

B. Third-Order In-Line NR-FPD

To validate the scalability of the real-time TD analysis of the proposed FDTD model for multiport networks, the 3rd-order in-line NR-FPD (Fig. 10) is evaluated under the same signal excitations.

1) Sinusoidal Signal Analysis: The NR-FPD is tested using continuous-wave tones at 1.2 GHz (in-band) and 1.1 GHz (out-of-band). In the forward direction ($P_1 \rightarrow P_2/P_3$), the frequency-domain responses [Figs. 20(a) and (b)] indicate strong transmission for the in-band signal, with minimal attenuation, while the out-of-band signal is significantly suppressed. This demonstrates the filter's ability to selectively pass signals within the designed passband. In the reverse direction ($P_2 \rightarrow P_1/P_3$), reduced transmission is observed for both frequencies

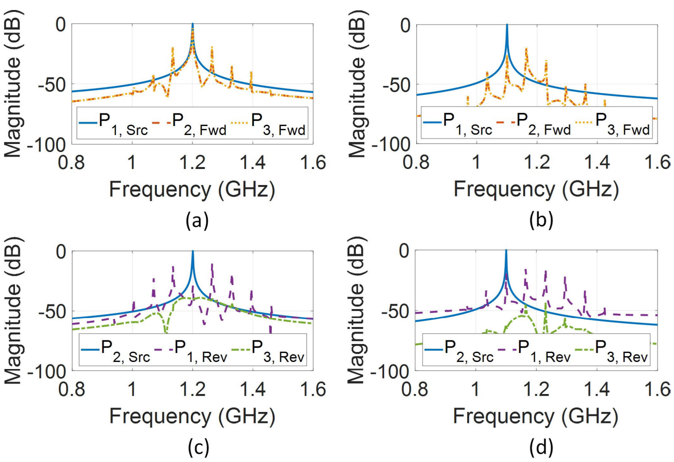

Fig. 20. Frequency-domain responses of the 3rd-order in-line NR-FPD to sinusoidal excitation. Forward propagation ($P_1 \rightarrow P_2/P_3$) at (a) 1.2 GHz (in-band) and (b) 1.1 GHz (out-of-band). Reverse propagation ($P_2 \rightarrow P_1/P_3$) at (c) 1.2 GHz (in-band) and (d) 1.1 GHz (out-of-band).

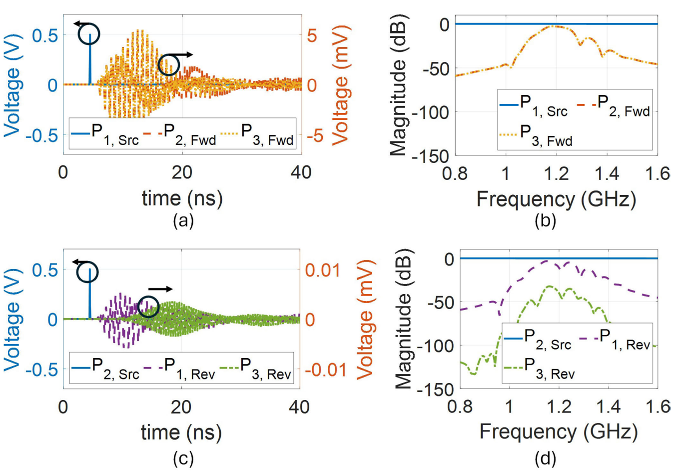

Fig. 21. Time- and frequency-domain responses of the 3rd-order in-line NR-FPD to a Gaussian pulse. (a) and (b) Forward propagation ($P_1 \rightarrow P_2/P_3$). (c) and (d) Reverse propagation ($P_2 \rightarrow P_1/P_3$).

[Fig. 20(c) and (d)], particularly for the out-of-band tone, confirming the circuit's NR and frequency-selective behavior.

2) Pulse Signal Analysis: A Gaussian pulse is applied at P_1 and P_2 to analyze its temporal behavior. In the forward case ($P_1 \rightarrow P_2/P_3$), waveforms at the output ports [Fig. 21(a)] and frequency responses [Fig. 21(b)] show confined energy in the passband. In the reverse ($P_2 \rightarrow P_1/P_3$) direction the outputs [Fig. 21(c)] exhibit broader spectra [Fig. 21(d)] and less isolation for $P_2 \rightarrow P_1$ propagation. As with the NR-BPF, the power divider redistributes spectral energy due to modulation, allowing partial signal transmission outside the passband while maintaining directionality.

3) QPSK Signal Analysis: A QPSK input [Fig. 22(a)] is applied at P_1, and outputs are recorded at P_2 and P_3 [Fig. 22(b) and (c)]. As it can be seen, the frequency-domain signals show minimal distortion, and the corresponding constellation diagrams [Fig. 23(b) and (c)] confirm good signal integrity with BERs 0. In the reverse direction (source at P_2), the output signals at P_1 and P_3 [Fig. 22(d) and (e)] exhibit degraded

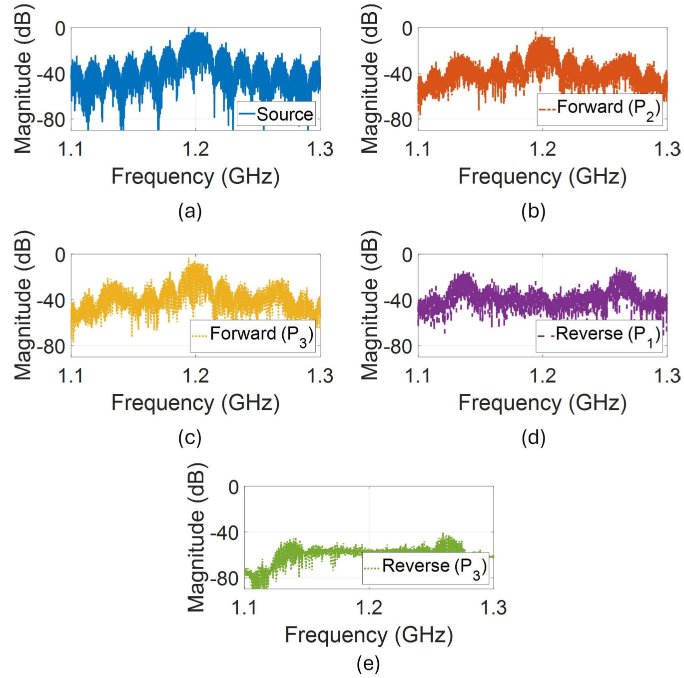

Fig. 22. Frequency-domain responses of the 3rd-order in-line NR-FPD to a QPSK modulated signal: (a) source, (b) forward at P_2, (c) forward at P_3, (d) reverse at P_1, and (e) reverse at P_3.

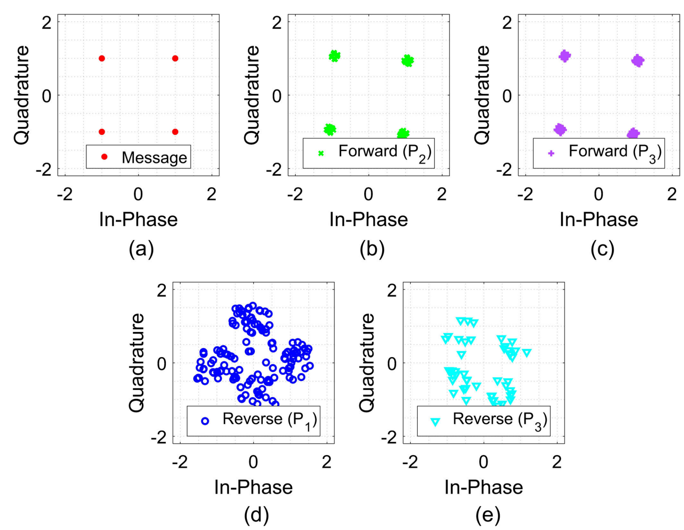

Fig. 23. Constellation diagrams of QPSK signals through the 3rd-order in-line NR-FPD. (a) Input, (b) and (c) forward ($P_1 \rightarrow P_2/P_3$), and (d) and (e) reverse ($P_2 \rightarrow P_1/P_3$).

spectra, and constellation diagrams [Fig. 23(d) and (e)] display severe distortion with BER 0.675 and 0.725, respectively. The RF degradation at P_1 confirms the NR performance, while the degradation at P_3 is due to the resistor in the power divider.

The FDTD simulations confirm the robust, direction-dependent behavior of both NR-circuits. Compared to HB methods, which are unsuitable for broadband, time-modulated systems, the FDTD framework supports transient, full-wave analysis of STM devices. These results affirm the method's value for the design and validation of advanced NR-RF components and communication systems.

This article has been accepted for inclusion in a future issue of this journal. Content is final as presented, with the exception of pagination.

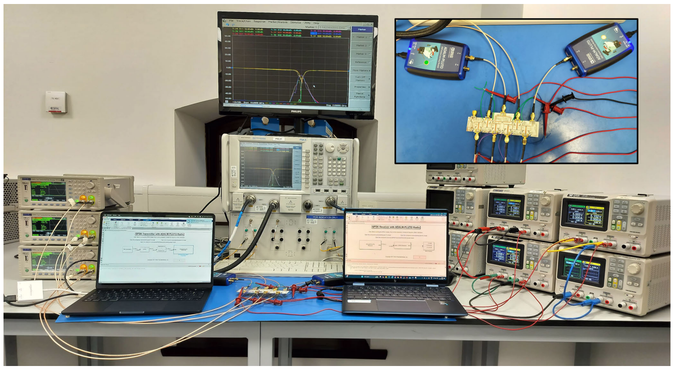

Fig. 24. Measurement setup for S-parameters, response to sinusoids, and QPSK constellation diagrams. S-parameters and response to sinusoids are measured using a Keysight PNA-X, and the QPSK constellation diagrams are measured by Analog Devices' Adalm Pluto SDRs.

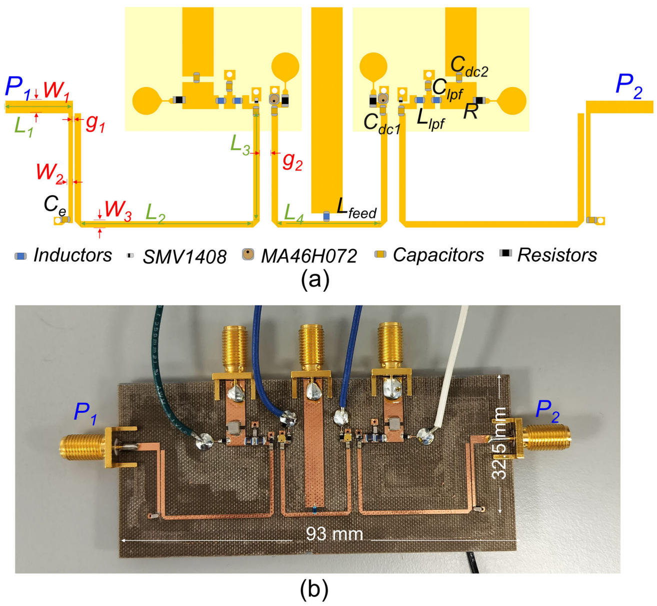

Fig. 25. (a) Layout and (b) photograph of the manufactured prototype of the 3[rd]-order in-line NR-BPF shown in Fig. 6. W_1 = 1.795, W_2 = 0.65, W_3 = 0.929, L_1 = 9.04, L_2 = 24.716, L_3 = 15.45, L_4 = 14.77, g_1 = 0.25, and g_2 = 1.7, all in mm. L_{lpf} = 50 nH, L_{feed} = 180 nH, C_{lpf} = 27 pF, C_{dc1} = 47 pF, C_{dc2} = 680 pF, C_e = 1.1 pF, and R = 10 MΩ.

VI. Experimental Validation

To further validate the proposed FDTD-based models for NR-circuits, prototypes of selected devices, including an in-line 3rd-order NR-BPF, a 4th-order transversal NR-BPF, and a 3rd-order in-line NR-FPD, were fabricated and measured. The S-parameters and response to sinusoids were characterized using a Keysight PNA-X, while all varactor-based time-modulated elements were driven by arbitrary waveform generators (AWGs), as shown in Fig. 24. The QPSK constellation diagrams were measured by Analog Devices' Adalm Pluto SDRs.

A. Third-Order In-Line NR-BPF

The manufactured 3rd-order in-line NR-BPF prototype is shown in Fig. 25. Measured S-parameters at two tuning

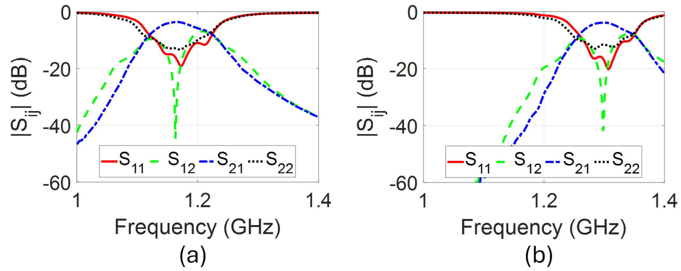

Fig. 26. RF-measured S-parameters for the 3rd-order in-line NR-BPF for center frequency tuned to (a) 1.164 and (b) 1.298 GHz.

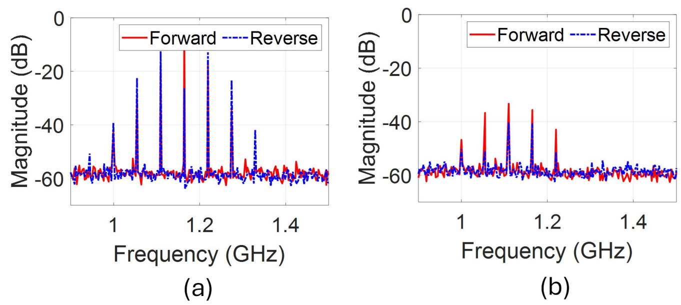

Fig. 27. Spectral response of the 3rd-order in-line NR-BPF (tuned to 1.164 GHz) to sinusoids at (a) 1.164 GHz (in-band) and (b) 1 GHz (out-of-band) in forward and reverse directions.

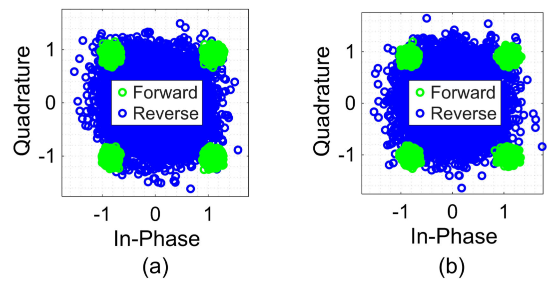

Fig. 28. Constellation diagrams of QPSK signals through the 3rd-order in-line NR-BPF. Forward and reverse at (a) 1.164 and (b) 1.298 GHz.

configurations are presented in Fig. 26. By adjusting the varactor biasing conditions, the center frequencies were set to 1.164 and 1.298 GHz. The results demonstrate strong direction-dependent behavior with clear frequency tunability. At 1.164 GHz, forward transmission exhibits an insertion loss of 3.62 dB, while reverse transmission is suppressed to −44.7 dB. At 1.298 GHz, forward loss is 3.83 dB, and reverse isolation reaches 41.83 dB. Single-tone tests further confirm this behavior (Fig. 27). When excited at 1.164 GHz (in-band), the forward transmission is maintained at −5.76 dB, whereas the reverse transmission is suppressed to −26.34 dB. At 1 GHz (out-of-band), both directions show strong rejection: 46.74 dB (forward) and 50.28 dB (reverse), confirming the filter's spectral selectivity. The filter's performance with modulated signals was assessed using QPSK waveforms. Constellation diagrams shown in Fig. 28 illustrate a well-defined forward reception at both center frequencies, with BERs of 0.01541 at 1.164 GHz [Fig. 28(a)] and 0.01085 at 1.298 GHz

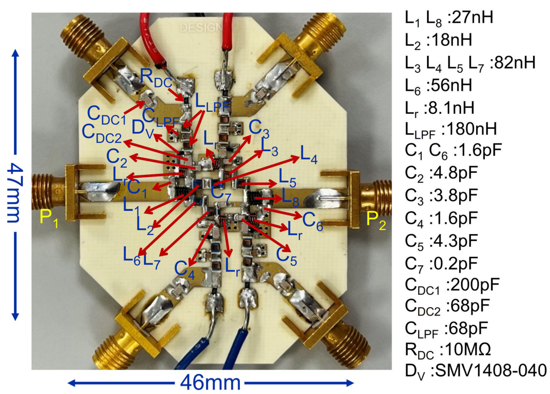

Fig. 29. Manufactured prototype of the transversal 4th-order single-band NR-BPF shown in Fig. 8 [24].

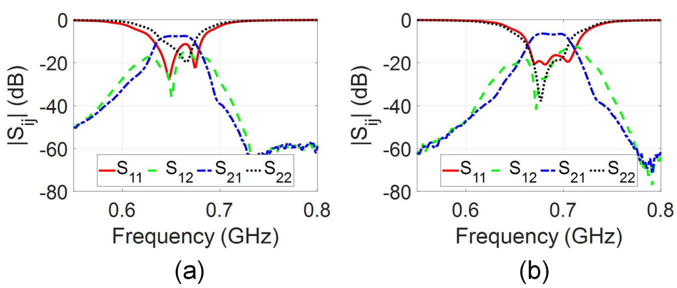

Fig. 30. RF-measured S-parameters of the transversal 4th-order single-band NR-BPF when its center frequency is tuned to (a) 654 and (b) 675 MHz.

[Fig. 28(c)]. In contrast, the reverse direction exhibits significant distortion, with BERs of 0.3338 and 0.458 for 1.164 GHz [Fig. 28(b)] and 1.298 GHz [Fig. 28(d)], respectively. These results validate the filter's NR operation, tunability, and robustness under complex modulation.

The measured results show good agreement with the simulations, with the main differences attributed to practical losses that were not included in the present FDTD models. Notably, this work demonstrates for the first time the use of the FDTD method to simulate NR-circuits with multiple junctions and multiple ports, as exemplified by the NR-FPD and the NR-filtering 3-dB coupler examples. To keep the initial demonstration simple, the FDTD simulations were carried out using linear and ideal components. If required, losses can be incorporated by introducing resistance (R) and conductance (G) into the Telegrapher's equations, starting from a lossy TL-unit cell.

B. Transversal Fourth-Order Single-Band NR-BPF

A fourth-order NR-BPF using transversal time-modulated resonators, shown in Fig. 8, was designed and manufactured, and its prototype is illustrated in Fig. 29. The implementation follows the component values and biasing conditions reported in [24]. Each resonator is an LC network loaded with a varactor and driven by a periodic modulation signal, enabling frequency tuning and NR operation. Measured S-parameters for center frequencies of 654 and 675 MHz are presented in Fig. 30. The results show forward insertion losses of 7.63 and 6.62 dB, and reverse attenuation levels of 36.44 and 41.82 dB, confirming strong directionality and tunable response.

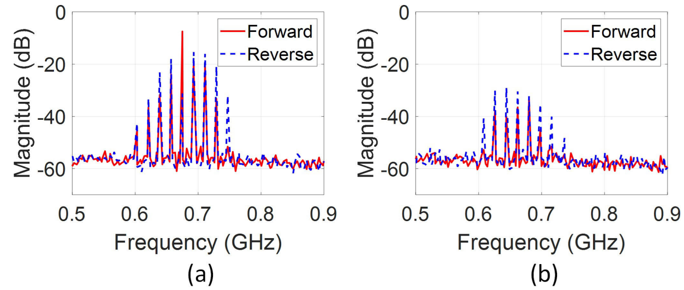

Fig. 31. Spectral response of the transversal 4th-order single-band NR-BPF (tuned to 675 MHz) to sinusoids at (a) 675 MHz (in-band) and (b) 662 MHz (out-of-band) in forward and reverse directions.

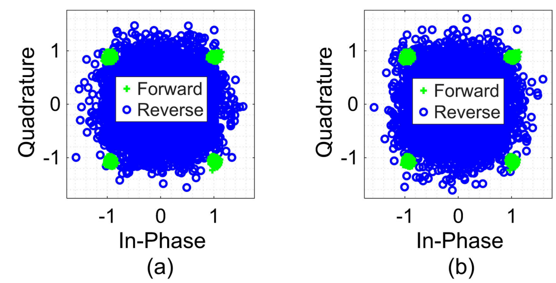

Fig. 32. QPSK constellation diagrams for the transversal 4th-order single-band NR-BPF when tuned to (a) 654 and (b) 675 MHz in forward and reverse directions, respectively.

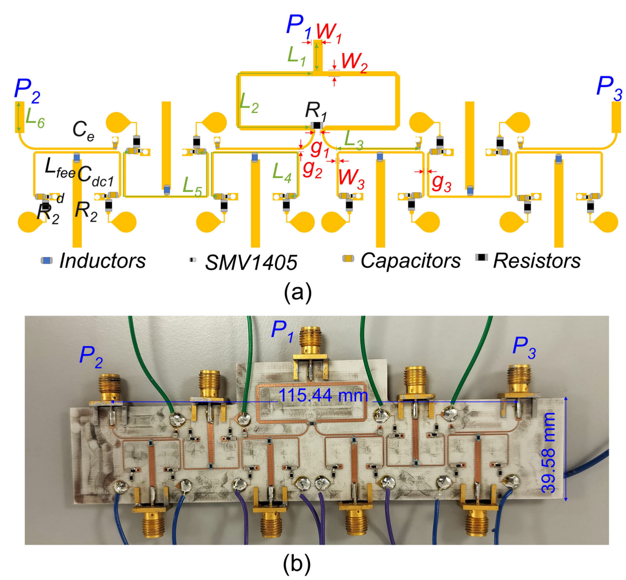

Fig. 33. (a) Layout and (b) the manufactured prototype of the 3rd-order in-line NR-FPD in Fig. 10. Design parameters (in mm): $W_1 = 1.79$, $W_2 = 0.93$, $W_3 = 0.44$, $L_1 = 6$, $L_2 = 38.3$, $L_3 = 15.5$, $L_4 = 35.66$, $L_5 = 35.16$, $L_6 = 6$, $g_1 = 1$, $g_2 = 0.25$, and $g_3 = 0.45$. $L_{feed} = 82$ nH, $C_{dc1} = 47$ pF, $C_e = 2$ pF, $R_1 = 100\ \Omega$, and $R_2 = 10$ MΩ.

TD measurements with single-tone excitations at 675 MHz (in-band) and 662 MHz (out-of-band) are shown in Fig. 31. Forward transmission at 675 MHz is suppressed by 7.48 dB, while the reverse is observed to be 31.2 dB. At 662 MHz, both directions show attenuation (36.53-dB forward and 30.46-dB

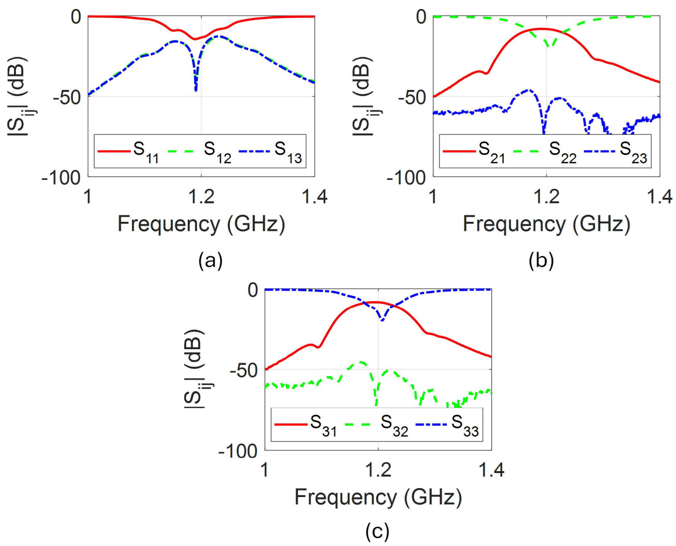

Fig. 34. RF-measured S-parameters of the 3[rd]-order in-line NR-FPD when tuned to 1.2 GHz. (a) S_{1j}, (b) S_{2j},3 and (c) S_{3j}, $j = 1, 2, 3$.

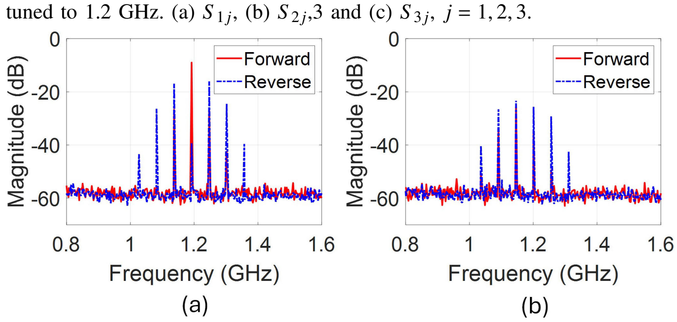

Fig. 35. Spectral response of the 3rd-order in-line NR-FPD to sinusoids at (a) 1.192 GHz (in-band) and (b) 1.09 GHz (out-of-band) in forward and reverse directions.

reverse), demonstrating spectral selectivity. QPSK waveform testing at both tuning configurations is presented in Fig. 32. Forward propagation yields clean constellation diagrams with BERs of 0.00373 [Fig. 32(a)] and 0.02355 [Fig. 32(c)]. In the reverse direction, significant distortion is observed, with BERs of 0.235 [Fig. 32(b)] and 0.4991 [Fig. 32(d)]. These measurements confirm the filter's efficacy for digitally modulated signals and its strong directional characteristics.

C. Third-Order In-Line NR-FPD

A 3rd-order NR-FPD was designed and manufactured based on in-line STM resonators, as shown in Fig. 33. The circuit topology corresponds to the configuration denoted as CRD in Fig. 10, utilizing varactor-loaded *LC* resonators modulated via synchronized AWGs. Measured S-parameters at 1.2 GHz are presented in Fig. 34.

As can be seen, the forward transmission from port P_1 to ports P_2 and P_3 exhibits an insertion loss of 8.3 dB. In the reverse direction, strong isolation is achieved, with suppression of 43.7 dB from P_2/P_3 to P_1. Single-tone testing results are shown in Fig. 35 for both in-band (1.192 GHz) and out-of-band (1.09 GHz) excitations. At 1.192 GHz, the forward and the reverse transmissions were measured −8.97 and −39.36 dB, respectively. At 1.09 GHz, attenuation is observed in both directions: 25.86 dB (forward) and 23.36 dB (reverse), confirming frequency selectivity and directionality. The NR-FPD's performance with modulated signals was evaluated using QPSK waveforms. Constellation diagrams for ports P_2 and P_3 in the forward direction [Fig. 36(a) and (b)] exhibit minimal distortion and a BER of 0.001539. In contrast, the reverse direction [Fig. 36(c) and (d)] shows heavily degraded constellations with BERs of 0.4983 and 0.4985, confirming the NR nature under modulated signal conditions.

These measurements confirm the FPD's directionality, tunability, and ability to handle complex waveforms. Alongside prior NR-BPF results, the measurement results validate the

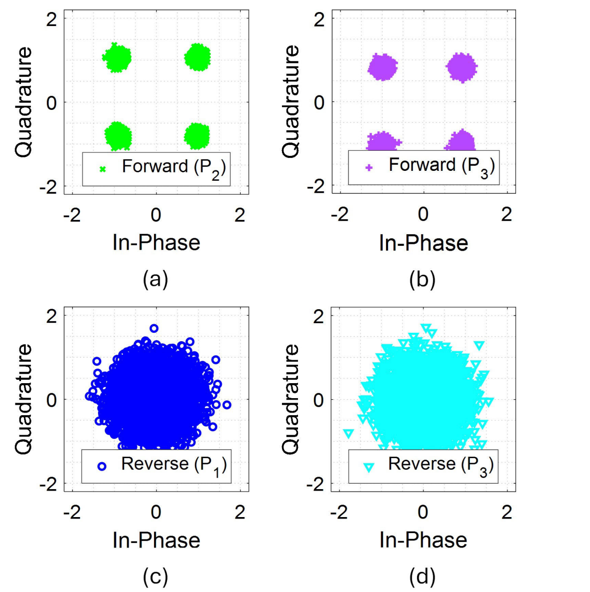

Fig. 36. Constellation diagrams for the 3rd-order in-line NR-FPD (tuned to 1.2 GHz) under QPSK excitation. Forward (a) $P_1 \rightarrow P_2$ and (b) $P_1 \rightarrow P_3$. Reverse (c) $P_2 \rightarrow P_1$ and (d) $P_2 \rightarrow P_3$.

TABLE II
COMPARISON OF MEMORY AND SIMULATION TIME FOR THE ADS-HB SIMULATIONS AND THE FDTD METHOD

Circuit (# Ports N_p)	**Method (# Harm. n_H)**	**S-parameter**		**Sinusoidal**		**Pulse**		**QPSK**	
		Mem. (MB)	**Time (s)**	**Mem. (MB)**	**Time (s)**	**Mem. (MB)**	**Time (s)**	**Mem. (MB)**	**Time (s)**
In-line 3[rd]-order NR-BPF ($N_p=2$)	ADS-HB (n_H=15)	48.1	28.6	47.4	11	NA	NA	NA	NA
	FDTD ($n_H \rightarrow \infty$)	4.5	36.9	12.12	5.9	14.78	4	115	66
Transversal 4[th]-order single-band NR-BPF ($N_p=2$)	ADS-HB (n_H=15)	50.8	35.7	49.6	12.2	NA	NA	NA	NA
	FDTD ($n_H \rightarrow \infty$)	5.1	42.3	14.2	6.4	16.9	4.6	128	72
In-line 3[rd]-order NR-FPD ($N_p=3$)	ADS-HB (n_H=15)	53.3	88.4	51	12	NA	NA	NA	NA
	FDTD ($n_H \rightarrow \infty$)	12.45	110.2	37.82	6.3	31.65	6.7	206	76
Transversal cell based NR-FPD ($N_p=3$)	ADS-HB (n_H=15)	86.7	202.3	82.8	24.2	NA	NA	NA	NA
	FDTD ($n_H \rightarrow \infty$)	34.1	225.4	61.6	17.1	65.2	17.5	332	182
3[rd]-order In-line NR-Filtering 3dB Coupler ($N_p=4$)	ADS-HB (n_H=15)	79.9	128.7	74.5	16.5	NA	NA	NA	NA
	FDTD ($n_H \rightarrow \infty$)	28.6	168.9	52.3	8.2	44.8	8.4	285	165

NA: Not Applicable

TABLE III
COMPARISON OF COMPUTATIONAL METHODS FOR MODELING STM CIRCUITS

Aspect	**Field-based FDTD** [33]	**Harmonic balance** [28]	**Spectral admittance matrix** [17], [18]	**Telegrapher's equations-based FDTD [This Work]**
Modelling approach	Solves Maxwell's equations on a spatial grid	Solves nonlinear steady-state equations in the frequency domain	Solves circuit response using harmonic-domain admittance representation	Solves circuit-level Telegrapher's equations in the time domain
Dimensionality	1D, 2D, 3D	1D/2D circuit netlists	1D	1D
Space-time-modulation fidelity	Fully capable of modeling arbitrary space-time variations in permittivity/permeability	Cannot directly model time-modulated media; approximates time variation using nonlinear controlled sources	Assumes periodicity; effective for steady-state analysis of STM systems	Efficient for TLs with periodic/arbitrary time-modulated L/C elements and their junctions
Computational cost	High, especially in 3D or fine-resolution domains	Efficient for nonlinear time-invariant circuits	Very efficient for linear periodic systems	Moderate; much faster than field-based FDTD for circuits
Modulation type	Arbitrary spatial, temporal, and spatio-temporal modulation	Limited to periodic space-time variation (Fourier-based expansion)	Limited to periodic space-time variation (Fourier-based expansion)	Arbitrary spatial, temporal, and spatio-temporal modulation
Nonlinearity	Incorporates nonlinear media or sources	Specialized for nonlinear sources/components	Only linear STM components are supported	Can incorporate nonlinear elements and/or sources
Scalability	Poor for large or complex circuits	Scales well for compact, time-invariant circuit models; complexity grows with the number of harmonics and ports	Moderate; complexity grows with the number of harmonics and ports	Good scalability with structured TL networks

robustness and versatility of the proposed FDTD framework for time-modulated NR-RF systems.

The measured insertion losses are slightly higher than the simulated values due to several practical factors not fully captured in the ideal FDTD model. These include the finite quality factor ($Q \approx$ 50–75) of the varactors, parasitic effects from DC biasing networks, fabrication tolerances in substrate parameters and component placement, and unmodeled parasitic reactances from solder joints and interconnections. Despite these factors, the measured results remain consistent with recent NR-filtering implementations [21], [22], [23], [24], [25], and the FDTD simulations accurately capture the key NR behavior, including isolation and transmission characteristics.

Table II summarizes the memory usage and simulation times of the proposed FDTD framework and the conventional ADS HB solver for all representative circuits considered in this work, including two-port, three-port, and four-port NR bandpass filters, filtering power dividers, and couplers. All simulations were performed on the same hardware platform (13th Gen Intel Core i7-1355U processor, 32-GB RAM) to ensure consistency.

For single-frequency S-parameter extraction, HB generally achieves faster simulation times; however, its memory consumption increases significantly with circuit complexity and port count. In contrast, the proposed FDTD method requires substantially less memory for S-parameter evaluation, despite inherently capturing an effectively infinite number of harmonics. For steady-state sinusoidal excitation, the FDTD approach demonstrates competitive or superior time performance for multiport circuits. Moreover, HB is not directly applicable to arbitrary waveform excitations such as pulses and QPSK signals, whereas the FDTD framework supports these within a single broadband TD simulation.

As circuit complexity increases, HB computational cost scales with harmonic order and nonlinear coupling, while FDTD cost scales primarily with spatial discretization. The proposed FDTD approach can be further optimized using parallel computing to reduce simulation time, making it even more attractive for large-scale circuit analysis. These results highlight the favorable scalability and broader applicability of the proposed approach for multiport space–time modulated circuit analysis.

Table III further contrasts major computational approaches for STM circuit modeling. Field-based FDTD methods offer full-wave modeling capabilities with high fidelity for arbitrary space–time modulation profiles but are computationally expensive, especially in 3-D. In contrast, HB and SAM methods operate in the frequency domain and are efficient for steady-state analysis but are limited to periodic STM systems and typically support only linear components. The proposed Telegrapher's equations-based FDTD approach achieves a favorable balance by enabling TD modeling of TL-based STM circuits with both arbitrary modulation schemes and nonlinear elements, offering good scalability and reduced computational overhead for circuit-level analysis. Key contributions of the proposed FDTD method include the following.

1) A TD solver for NR-circuits using modified Telegrapher's equations with embedded lumped-element time-modulated resonators.
2) A novel TL junction modeling approach with custom BCs to support multiport interconnections.
3) Support for arbitrary excitation waveforms, including single tones, pulses, and digitally modulated signals (e.g., QPSK), and extraction of comprehensive performance metrics such as S-parameters, spectra, TD waveforms, and constellation diagrams from a single simulation run.

VII. CONCLUSION

This article presented a generalized FDTD-based framework for the TD analysis and design of multiport NR microwave circuits composed of STM resonators and interconnected TL junctions. By extending classical Telegrapher's equations and incorporating time-varying lumped-element models, the proposed method enables accurate full-wave transient simulation of STM RF systems without relying on steady-state assumptions or harmonic truncation, which are inherent limitations of frequency-domain approaches such as HB simulations. The proposed method was validated through a suite of NR-circuits, including in-line and transversal NR-BPFs, NR-FPDs, and NR-couplers. Simulation results showed excellent agreement with both HB simulations and experimental measurements, capturing key phenomena such as direction-dependent transmission and frequency selectivity. Real-time tests with QPSK waveforms confirmed the solver's ability to assess NR behavior under complex modulated signal conditions, demonstrating preserved forward signal integrity and strong reverse suppression in constellation diagrams.

Compared to HB-based methods, the FDTD framework offers several advantages: it captures all harmonics inherently, supports broadband transient analysis, and facilitates realistic signal-level evaluation of NR-circuits without requiring physical hardware. These capabilities make it a powerful tool for the design of next-generation reconfigurable and NR microwave systems. Future work will focus on extending the framework to include co-simulation with EM solvers for hybrid passive–active circuit design and exploring its integration into automated synthesis and optimization workflows for advanced NR devices.

Appendix
FDTD Algorithms

This appendix summarizes the high-level algorithms used for S-parameter extraction and TD analysis of NR multiport circuits within the proposed FDTD framework.

References

[1] P. Dutta, G. Arun Kumar, G. Ram, and D. Suneel Varma, "Spatiotemporal nonreciprocal filters: Theoretical concepts and literature review," *IEEE Microw. Mag.*, vol. 23, no. 6, pp. 85–101, Jun. 2022.

[2] A. Nagulu and H. Krishnaswamy, "Non-magnetic non-reciprocal microwave components—State of the art and future directions," *IEEE J. Microw.*, vol. 1, no. 1, pp. 447–456, Jan. 2021.

[3] S. Taravati, "Aperiodic space-time modulation for pure frequency mixing," *Phys. Rev. B, Condens. Matter*, vol. 97, no. 11, Mar. 2018, Art. no. 115131.

[4] A. Nagulu, N. Reiskarimian, and H. Krishnaswamy, "Non-reciprocal electronics based on temporal modulation," *Nature Electron.*, vol. 3, no. 5, pp. 241–250, May 2020.

[5] M. G. Ahmed, M. M. M. Ali, S. I. Shams, M. Elsaadany, and A. M. M. A. Allam, "Ferrite isolator based on dual non-reciprocal mode converting in rectangular waveguide," in *Proc. 15th Eur. Conf. Antennas Propag. (EuCAP)*, Dusseldorf, Germany, Mar. 2021, pp. 1–4.

[6] J. Silverman, "Nonreciprocal behavior in passive systems," *IRE Trans. Compon. Parts*, vol. 9, no. 2, pp. 77–81, Jun. 1962.

[7] C. Surawatpunya, "Nonreciprocal filter behavior in a periodic edge-loaded ferrite microstripline," *Proc. IEEE*, vol. 74, no. 1, pp. 215–216, 1986.

[8] Y. Shoji and T. Mizumoto, "Magneto-optical non-reciprocal devices in silicon photonics," *Sci. Technol. Adv. Mater.*, vol. 15, no. 1, Feb. 2014, Art. no. 014602.

[9] H. Zhu and M. Rais-Zadeh, "Non-reciprocal acoustic transmission in a GaN delay line using the acoustoelectric effect," *IEEE Electron Device Lett.*, vol. 38, no. 6, pp. 802–805, Jun. 2017.

[10] J. Wu, X. Yang, S. Beguhn, J. Lou, and N. X. Sun, "Nonreciprocal tunable low-loss bandpass filters with ultra-wideband isolation based on magnetostatic surface wave," *IEEE Trans. Microw. Theory Techn.*, vol. 60, no. 12, pp. 3959–3968, Dec. 2012.

[11] H. M. Jeon, K. Brockdorf, B. M. Howe, J. Myers, S. Mou, and Y. Zhuang, "Propagation of non-reciprocal magnetostatic surface wave in a 20-nm-thick single crystalline yttrium iron garnet film," *IEEE Electron Device Lett.*, vol. 38, no. 2, pp. 262–265, Feb. 2017.

[12] X.-H. Li, H.-M. Zhou, Q.-S. Zhang, and W.-W. Hu, "Lumped modeling with circuit elements for nonreciprocal magnetoelectric tunable band-pass filter," *Chin. Phys. B*, vol. 25, no. 11, Nov. 2016, Art. no. 117505.

[13] M. Ghatge, G. Walters, T. Nishida, and R. Tabrizian, "A non-reciprocal filter using asymmetrically transduced micro-acoustic resonators," *IEEE Electron Device Lett.*, vol. 40, no. 5, pp. 800–803, May 2019.

[14] S. Poddar, A. M. Holmes, and G. W. Hanson, "Design and analysis of an electronically tunable magnet-free non-reciprocal metamaterial," *IEEE Trans. Antennas Propag.*, vol. 70, no. 8, pp. 7311–7315, Aug. 2022.

[15] Q. Gu, X. Zheng, Y. Zhou, F. Sun, and S. Liu, "A 2.5D broadband non-reciprocal metasurface based on aperture-coupled feed structures," *IEEE Access*, vol. 11, pp. 104858–104865, 2023.

[16] S. Qin, Q. Xu, and Y. E. Wang, "Nonreciprocal components with distributedly modulated capacitors," *IEEE Trans. Microw. Theory Techn.*, vol. 62, no. 10, pp. 2260–2272, Oct. 2014.

[17] X. Wu, X. Liu, M. D. Hickle, D. Peroulis, J. S. Gómez-Díaz, and A. Álvarez Melcón, "Isolating bandpass filters using time-modulated resonators," *IEEE Trans. Microw. Theory Techn.*, vol. 67, no. 6, pp. 2331–2345, Jun. 2019.

[18] A. Alvarez-Melcon, X. Wu, J. Zang, X. Liu, and J. S. Gomez-Diaz, "Coupling matrix representation of nonreciprocal filters based on time-modulated resonators," *IEEE Trans. Microw. Theory Techn.*, vol. 67, no. 12, pp. 4751–4763, Dec. 2019.

[19] D. Simpson and D. Psychogiou, "Fully-reconfigurable non-reciprocal bandpass filters," in *IEEE MTT-S Int. Microw. Symp. Dig.*, Aug. 2020, pp. 807–810.

[20] P. Dutta, G. A. Kumar, and G. Ram, "Numerical design of non-reciprocal bandpass filters with the aid of 3D coupling matrix for 5G bands," *IEEE Trans. Circuits Syst. II, Exp. Briefs*, vol. 69, no. 7, pp. 3334–3338, Jul. 2022.

[21] D. Simpson, P. Vryonides, S. Nikolaou, and D. Psychogiou, "Non-reciprocal balanced bandpass filters with quasi-elliptic response," *IEEE Trans. Circuits Syst. II, Exp. Briefs*, vol. 69, no. 12, pp. 5159–5163, Dec. 2022.

[22] X. Wu, M. Nafe, A. A. Melcon, J. S. Gomez-Diaz, and X. Liu, "Frequency tunable non-reciprocal bandpass filter using time-modulated microstrip $\lambda_g/2$ resonators," *IEEE Trans. Circuits Syst. II, Exp. Briefs*, vol. 68, no. 2, pp. 667–671, Feb. 2021.

[23] A. Ashley and D. Psychogiou, "X-band quasi-elliptic non-reciprocal bandpass filters (NBPFs)," *IEEE Trans. Microw. Theory Techn.*, vol. 69, no. 7, pp. 3255–3263, Jul. 2021.

[24] Z. Zhang and D. Psychogiou, "Incorporating directionality in transversal-resonator-based bandpass filters with tunable transfer function characteristics," *IEEE Trans. Circuits Syst. I, Reg. Papers*, vol. 70, no. 12, pp. 5194–5207, Dec. 2023.

[25] J. Zang, S. Wang, A. Alvarez-Melcon, and J. S. G. Diaz, "Non-reciprocal filtering power dividers," *AEU-Int. J. Electron. Commun.*, vol. 132, 2021, Art. no. 153609.

[26] S. Taravati and C. Caloz, "Mixer-duplexer-antenna leaky-wave system based on periodic space-time modulation," *IEEE Trans. Antennas Propag.*, vol. 65, no. 2, pp. 442–452, Feb. 2017.

[27] J. T. S. Do, J. Zang, A. Alvarez-Melcon, and J. S. Gomez-Diaz, "Time-modulated patch antennas with tunable and nonreciprocal polarization response," *IEEE Access*, vol. 10, pp. 59057–59067, 2022.

[28] *Harmonic Balance Simulation*, Advance Design System, Feb. 2011.

[29] G. Chaudhary, Y. Meng, D. Sun Park, and Y. Jeong, "Attention-based deep neural network for high-dimensional microwave modeling of non-reciprocal bandpass filters," *IEEE Access*, vol. 13, pp. 56220–56236, 2025.

[30] J. Li, C. Shen, X. Zhu, Y. Xie, and S. A. Cummer, "Nonreciprocal sound propagation in space-time modulated media," *Phys. Rev. B, Condens. Matter*, vol. 99, no. 14, Apr. 2019, Art. no. 144311.

[31] J. R. Zurita-Sánchez, P. Halevi, and J. C. Cervantes-González, "Reflection and transmission of a wave incident on a slab with a time-periodic dielectric function $\epsilon(t)$," *Phys. Rev. A, Gen. Phys.*, vol. 79, no. 5, May 2009, Art. no. 053821.

[32] D. Sarkar, *FDTD Analysis of Guided Electromagnetic Wave Interaction With Time-Modulated Dielectric Medium*. Cham, Switzerland: Springer, 2022.

[33] A. Kumar and D. Sarkar, "FDTD analysis of space-time metamaterials using modulated TVTLs for frequency translation, mixing and non-reciprocity," in *Proc. 53rd Eur. Microw. Conf. (EuMC)*, Berlin, Germany, Sep. 2023, pp. 311–314.

[34] M. Q. Dinh and M. Thuy Le, "Surface plasmon polaritons in time-modulated metallic materials for non-reciprocal controllable leaky-wave antennas," *IEEE Access*, vol. 10, pp. 28461–28470, 2022.
[35] Z. He, H. Lu, and J. Zhao, "Polarization independent and non-reciprocal absorption in multi-layer anisotropic black phosphorus metamaterials," *Opt. Exp.*, vol. 29, no. 14, pp. 21336–21347, 2021.
[36] M. Fujii, A. Maitra, C. Poulton, J. Leuthold, and W. Freude, "Non-reciprocal transmission and Schmitt trigger operation in strongly modulated asymmetric WBGs," *Opt. Exp.*, vol. 14, no. 26, pp. 12782–12793, 2006.
[37] A. Kumar and D. Sarkar, "Insights into the non-reciprocal behavior of lossy space-time varying transmission lines using analytical and FDTD modeling," *Authorea Preprints*, Oct. 2025.
[38] A. Kumar, J. C. Dash, and D. Sarkar, "Computational techniques for design and analysis of time-varying capacitor loaded transmission lines using FDTD and simulink," *IEEE J. Multiscale Multiphys. Comput. Techn.*, vol. 7, pp. 228–235, 2022.
[39] A. Kumar, S. Kongari, Y. Chandrakapure, and D. Sarkar, "Multi-functional metasurface as a transmissive/reflective FSS and an on-air frequency mixer," *Sci. Rep.*, vol. 14, no. 1, p. 13874, Jun. 2024.
[40] A. Kumar, J. C. Dash, and D. Sarkar, "FDTD analysis of transmission line loaded with time-varying shunt capacitors for mixer applications," in *Proc. IEEE Int. Conf. Electron.*, Feb. 2022, pp. 1–6.
[41] A. Kumar, Z. Zhang, D. Sarkar, S. Nikolaou, P. Vryonides, and D. Psychogiou, "FDTD modeling of time-modulated resonators-based bandpass filters using modified telegrapher's equations," in *IEEE MTT-S Int. Microw. Symp. Dig.*, 2024, pp. 612–615.
[42] X. Zhong, K. K. Mei, and Y. Liu, "Application of online FDTD on microstrip cross and T-junction structures," *Microw. Opt. Technol. Lett.*, vol. 36, no. 3, pp. 184–187, Feb. 2003.
[43] Z. Yang and E. L. Tan, "Interconnected multi-1-D FADI- and FLOD-FDTD methods for transmission lines with interjunctions," *IEEE Trans. Microw. Theory Techn.*, vol. 65, no. 3, pp. 684–692, Mar. 2017.
[44] X. Wu, J. Ji, and Z. Ye, "Time domain hybrid method for the coupling analysis of transmission line with junctions," in *Proc. Int. Symp. Antennas Propag. Soc., Merging Technol.*, 2021, pp. 1–3.
[45] Y. Wang, J. Wang, L. Yao, and W.-Y. Yin, "EMI analysis of multiscale transmission line network using a hybrid FDTD method," *IEEE Trans. Electromagn. Compat.*, vol. 63, no. 4, pp. 1202–1211, Aug. 2021.
[46] X. Wang and R. J. Hwu, "Theoretical analysis and FDTD simulation of GaAs nonlinear transmission lines," *IEEE Trans. Microw. Theory Techn.*, vol. 47, no. 7, pp. 1083–1091, Jul. 1999.
[47] J.-S. G. Hong and M. J. Lancaster, *Microstrip Filters for RF/Microwave Applications*. Hoboken, NJ, USA: Wiley, 2004.
[48] X. Chen, M. Salek, Q. Zhang, and Y. Wang, "Subterahertz filtering six-port junction," *IEEE Trans. Microw. Theory Techn.*, vol. 70, no. 8, pp. 3877–3885, Aug. 2022.

Anand Kumar (Graduate Student Member, IEEE) received the B.Tech. degree (Hons.) in electronics and communication engineering from IIT (ISM) Dhanbad, Dhanbad, India, in 2020. He is currently pursuing the Ph.D. degree in electrical communication engineering at Indian Institute of Science (IISc), Bengaluru, India.

He is a Visiting Student at the Tyndall National Institute, University College Cork, Cork, Ireland. His research interests encompass computational electromagnetic methods, such as FDTD to model and analyze media with spatial and temporal dependence, MIMO antennas, and radar systems.

Mr. Kumar received the prestigious Prime Minister's Research Fellowship (PMRF) from the Ministry of Education, Government of India, in 2022, and was awarded the IEEE Antennas and Propagation Society Fellowship in 2023 and the IEEE Microwave Theory and Technology Society Graduate Student Fellowship in 2024.

Zixiao Zhang (Graduate Student Member, IEEE) received the bachelor's and master's degrees from the Huazhong University of Science and Technology, Wuhan, China, in 2016 and 2019, respectively. She is currently pursuing the Ph.D. degree in electrical and electronic engineering at University College Cork (UCC), Cork, Ireland.

Her current research interests include synthesis, design, and characterization of reconfigurable RF components.

Debdeep Sarkar (Senior Member, IEEE) received the B.E. degree in Electronics and Telecommunication Engineering (ETCE) from Jadavpur University, Kolkata, India, in 2011, and the M.Tech. and Ph.D. degrees in electrical engineering with specialization in RF and microwaves from IIT Kanpur, Kanpur, India, in 2013 and 2018, respectively.

He was a Visiting Researcher and a Post-Doctoral Fellow with the Department of Electrical and Computer Engineering, Royal Military College, Kingston, ON, Canada, from May 2017 to August 2017 and from 2018 to 2020, respectively. After that, he was an Assistant Professor with the Department of Electrical Engineering, IIT Ropar, Bara Phool, India, from March 2020 to July 2020. Since August 2020, he has been an Assistant Professor with the Department of Electrical Communication Engineering (ECE), Indian Institute of Science (IISc), Bengaluru, India. He has one book, one book chapter, three filed Indian patents, 48 peer-reviewed journals, and more than 100 conference papers to his credit.

Dr. Sarkar is currently a member of the IEEE AP-S Global YP Committee. He is an active reviewer of multiple prestigious IEEE TRANSACTIONS and IEEE letters and an Associate Editor of IET MAP and IEEE ACCESS. He was a recipient of the URSI Young Scientist Award twice (APRASC-2019 and GASS-2020), the Infosys Young Investigator Award during 2020–2022, the Outstanding YP (Young Professional) Volunteer Award in 2021 from the IEEE Bangalore Section, the IETE Sri C Viswanatha Reddy Memorial Award in 2022, and many other best-paper awards.

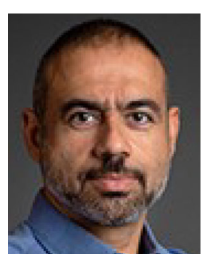

Symeon Nikolaou (Senior Member, IEEE) received the B.S. degree in electrical and computer engineering from the National Technical University of Athens, Athens, Greece, in 2003, and the M.S. and Ph.D. degrees in electrical and computer engineering from Georgia Institute of Technology, Atlanta, GA, USA, in 2005 and 2007, respectively.

He is currently a Professor with Frederick University, Nicosia, Cyprus, where he is a Senior Researcher with the Frederick Research Center. His research interests include the design of smart antennas, RFIDs/sensors, wearable and implantable antennas, and reconfigurable components for wireless transceivers.

Dr. Nikolaou is a member of the Technical Chamber of Cyprus and has been Cyprus' Delegate in the Management Committee of COST IC0603 Antenna Systems and Sensors for Information Society Technology (ASSIST) Action and the substitute Delegate for Cyprus' Substitute Delegate in the Management Committee of COST IC1102 Action on Versatile, Integrated, and Signal-Aware Technologies for Antennas (VISTA) Action. He is also serving as Cyprus' Delegate in the Management Committee of COST MiMED 1301 Accelerating the Technological, Clinical, and Commercialization Progress in the area of medical microwave imaging. He serves as a reviewer for IEEE TRANSACTIONS ON ANTENNAS AND PROPAGATION, IEEE TRANSACTIONS ON ADVANCED PACKAGING, IEEE ANTENNAS AND WIRELESS PROPAGATION LETTERS, and *Electronics Letters* (IET). He is also an Associate Editor of *IET Microwaves, Antennas and Propagation* and *International Journal of Antennas and Propagation*.

Photos Vryonides (Senior Member, IEEE) received the B.Eng., M.Phil., and Ph.D. degrees in electrical and electronic engineering from the University of Manchester Institute of Science and Technology (UMIST), Manchester, U.K., in 1998, 1999, and 2002, respectively.

He is currently an Associate Professor with Frederick University, Nicosia, Cyprus, where he is a Senior Researcher with the Frederick Research Center (FRC). He is a member with the Antennas and Microwaves Research Group, Frederick University, Nicosia. He has authored or co-authored more than 80 papers in journals and peer-reviewed conferences. His research interests include RF design and characterization of reconfigurable microwave and millimeter-wave passive components and antennas, and tunable filter synthesis.

Dr. Vryonides is a member of the Technical Chamber of Cyprus. He has been a Cyprus Delegate in the Management Committee of COST IC0803 (RF/Microwave Communication Subsystems for Emerging Technologies) Action and CA18223 (Future Communications with Higher Symmetric Engineered Artificial Materials). He serves as an Associate Editor for IEEE ACCESS and IEEE OPEN JOURNAL OF CIRCUITS AND SYSTEMS.

Dimitra Psychogiou (Senior Member, IEEE) received the Dipl.-Eng. degree in electrical and computer engineering from the University of Patras, Patras, Greece, in 2008, and the Ph.D. degree in electrical engineering from the Swiss Federal Institute of Technology (ETH), Zürich, Switzerland, in 2013.

She is currently a Full Professor (Chair) of microwave communications at the School of Engineering, University College Cork (UCC), Cork, Ireland, and the Head of the Advanced RF Technology Group, Tyndall National Institute, Cork. Prior to joining UCC, she was a Senior Research Scientist with Purdue University, West Lafayette, IN, USA, and an Assistant Professor with the University of Colorado Boulder, Boulder, CO, USA. Her research has been presented in more than 250 scientific publications. Her current research interests include RF design and characterization of reconfigurable microwave and millimeter-wave RF passive and active components, RF-MEMS, acoustic wave resonator-based filters, tunable filter synthesis, frequency-agile antennas, and additive manufacturing technologies for 3-D antenna subsystems.

Dr. Psychogiou is a Senior Member of URSI and a member of the IEEE MTT-S Filters and Passive Components (MTT-5) and Microwave Control Materials and Devices (MTT-13) Committees. She has received multiple awards, including the 2023 IEEE MTT-S Outstanding Young Engineer Award, the 2021 Roberto Sorrentino Prize, the SFI Research Professorship Award, the 2020 NSF CAREER Award, the 2020 URSI Young Scientist Award, and the Junior Faculty Outstanding Research Award from UC Boulder. She is currently serving as the President for URSI Ireland, the Vice-Chair for MTT-13, and a Secretary for USNC-URSI Commission D. He is also serving as a Pre-Screening Editor for IEEE JOURNAL OF MICROWAVES and an Associate Editor for *International Journal of Microwave and Wireless Technologies* and is on the technical review board of various IEEE and EuMA conferences. Previously, she was an Associate Editor of IEEE MICROWAVE WIRELESS TECHNOLOGY LETTERS and the *IET Microwaves, Antennas and Propagation* journal.